STAFF
REPORTS

NO. 1049
FEBRUARY 2023

REVISED
AUGUST 2024

Sparse Trend Estimation

Richard K. Crump | Nikolay Gospodinov | Hunter Wieman

FEDERAL RESERVE BANK of NEW YORK

Sparse Trend Estimation

Richard K. Crump, Nikolay Gospodinov, and Hunter Wieman

Federal Reserve Bank of New York Staff Reports, no. 1049
February 2023; revised August 2024
JEL classification: C13, C30, C33, E27, E32

Abstract

The low-frequency movements of economic variables play a prominent role in policy analysis and decision-making. We develop a robust estimation approach for these slow-moving trend processes which is guided by a judicious choice of priors and is characterized by sparsity. We present novel stylized facts from longer-run survey expectations that inform the structure of the estimation procedure. The general version of the proposed Bayesian estimator with a spike-and-slab prior accounts explicitly for cyclical dynamics. We show that it performs well in simulations against relevant benchmarks and report empirical estimates of trend growth for U.S. output and annual mean temperature.

Key words: slow-moving trends, sparsity, Bayesian inference, latent variable models, trend output growth

---

Crump: Federal Reserve Bank of New York (email: richard.crump@ny.frb.org). Gospodinov: Federal Reserve Bank of Atlanta (email: niko-lay.gospodinov@atl.frb.org). Wieman: Princeton University (email: hw8318@princeton.edu). This paper was previously circulated under the title "Elusive 'Stars': Robust Trend Estimation." The authors thank Serena Ng for detailed and constructive discussions on this project, editor Olivier Coibion, three anonymous referees, Martín Almuzara, Marco Del Negro, Domenico Giannone, and Alex Thorp. The authors also thank the seminar participants at the 2023 Montreal Econometrics Seminar series and the 2021 NBER Summer Institute for helpful comments and discussions, as well as Miro Everaert and Ignacio Lopez Gaffney for excellent research assistance.

1 Introduction

Quantifying and characterizing the low-frequency behavior of time series processes has a long tradition in economics. The appeal of constructing accurate and robust estimates for the slow-moving trend component of an economic series for informing policy analysis cannot be overstated. However, as the true low-frequency component is inherently unobserved, its extraction and validation for guiding economic policy is fraught with difficulties arising from substantial underlying uncertainty.

The commonly employed state-space approach essentially assumes a particular parametric structure about the deterministic and stochastic trend components, but it tends to exhibit fragilities to potential misspecification and imposes strong identification requirements. For example, it is often the case that even a seemingly innocuous misspecification in the trend component can induce a severe distortion in the estimated trend-cycle decomposition by erroneously attributing some of the low-frequency persistence to the cyclical dynamics. On the other hand, adopting a more agnostic approach by starting from an unrestricted set of nonparametric estimators may produce highly uncertain estimates that are of little practical relevance. This suggests that to achieve more informative inference, one may need to impose discipline on the low-frequency movements via prior information that ensure sparsity.

To inform our approach to trend estimation, we present novel survey evidence on "longer-run" forecasts – which offer a convenient way to define the low-frequency or trend component – of key variables of interest in the U.S. In addition to the "slow-moving" nature of these forecasts, we also provide a new stylized fact, summarized by histograms for the first and second difference of the forecast, that individual forecasters appear to change their long-run forecasts only rarely. To accommodate these features – slowly-evolving and infrequently-changing low-frequency component – we rely on sparsity and shrinkage through our choice of a spike-and-slab prior. This prior information that we impose on the unobserved trend process is intuitive and aligns with the beliefs of professional forecasters. To allow for high-frequency cyclical fluctuations, we employ a stationary autoregressive process. We implement

these ideas by resorting to the Bayesian counterpart of generalized LASSO estimation with separate penalties on the long-run and short-run components. Our method thus generalizes some existing procedures for robust trend estimation (Kim, Koh, Boyd, and Gorinevsky 2009, Tibshirani 2014, and Roualdes 2015) with the aim of capturing the salient features of economic data.

Prominent contributions to the study of the low-frequency behavior of economic series include Hodrick and Prescott (1980), Beveridge and Nelson (1981), Baxter and King (1999), Morley, Nelson, and Zivot (2003), among many others. A primary motivation of this literature is to isolate the low-frequency, slow-moving component of a series – which reflects the secular and structural factors that underlie its dynamic behavior – from its high-frequency, possibly cyclical, variations. Potential output, natural rate of unemployment, neutral real rate of interest, inflation expectations, and common variation in real activity are only a few examples of such slow-moving latent processes that are often denoted by and referred to as "stars." There are numerous papers that have implemented these methodologies in a wide range of applications across economics and finance (see, for example, Laubach and Williams 2003, Holston, Laubach, and Williams 2017, Del Negro, Giannone, Giannoni, and Tambalotti 2018, Crump, Eusepi, Giannoni, and Şahin 2019 among many others). There is also a well-established Bayesian literature tailored to trend estimation, e.g., Koop and Potter (2007), Harvey, Trimbur, and Van Dijk (2007), Grant and Chan (2017b,a), Kamber, Morley, and Wong (2018), and this larger research agenda continues to evolve with recent work such as Hamilton (2018), Phillips and Shi (2020), Lee, Liao, Seo, and Shin (2021), and Eo and Morley (2022) (see Hodrick 2020 and Canova 2023 for a comprehensive discussion).

The point of departure of this paper from the existing literature is to operationalize the "slow-moving" trend assumption through an imposition of sparsity that is informed by survey evidence of financial market participants. In particular, our contributions can be summarized as follows. First, we provide novel evidence on individual survey forecasts of the trend component of key economic variables. We utilize non-public data from the Survey of

Primary Dealers which is the only survey of professional forecasters which explicitly solicits longer-run forecasts on a consistent basis. Our matched panel data allows us to characterize the distribution of adjustments to longer-run forecasts over time. On the methodological side, we contribute to the literature on Bayesian sparse trend estimation by utilizing spike-and-slab priors and a serially correlated cycle component. The embedded sparsity of our estimator offers an alternative statistical characterization of a "slow-moving" trend. Furthermore, our Bayesian setup allows us to incorporate uncertainty around our estimates in an internally consistent manner. Finally, it is important to note that our approach is data-driven and adapts flexibly to the underlying structure of the data-generating process.

Our main empirical application focuses on the estimation of the low-frequency trend in real GDP growth. This is a perennial question in empirical macroeconomics with important implications for monetary and fiscal policy (for recent contributions, see, e.g., Fernald, Hall, Stock, and Watson 2017, Coibion, Gorodnichenko, and Ulate 2018 and Müller, Stock, and Watson 2020). Our estimates for 1947–2023 suggest that trend real GDP growth in the U.S. has been falling since the 1960s and ends the sample at 2.16%. Importantly, our method produces slow-moving trend estimates which do not systematically co-vary with the business cycle. We contrast our estimates to those based on recently proposed estimators. We further provide a detailed analysis of the underlying trend in the contributions to real GDP growth from its constituent components. Despite the fact that these components generally exhibit different dynamic properties, we find that the individual trends estimated for the GDP contributions can be aggregated and match closely the direct trend estimate from headline real GDP growth. We also explore another empirical application based on mean temperature changes in the U.S. over the last 140 years. We find strong evidence of a sustained rise in trend temperatures above the ecological targets over the last 45 years.

This paper is organized as follows. In Section 2, we provide heuristic motivation, based on long-run survey forecasts, for our general estimation approach which is introduced in Section 3. Section 4 assesses the finite-sample properties of our method across several sim-

ulation designs. Our main empirical applications, which investigate the trend in U.S. mean temperature and the trend in U.S. real GDP growth, are provided in Section 5. Section 6 concludes. Finally, the Appendix provides full details on the implementation of our proposed methodology and a Supplemental Appendix (hereafter, "SA") contains additional results.

2 Evidence on Survey-Based Trends

In this section, we present new stylized facts about longer-run survey forecasts of professional forecasters. This empirical evidence will serve as a motivation for the methodological approach that we introduce later in the paper. To cement ideas, it is useful to discuss a convenient mathematical formulation of an underlying trend (Beveridge and Nelson, 1981) of a variable y_t as $\lim_{h\to\infty} \mathbb{E}[y_{t+h}|\,\mathcal{F}_t]$, where $\mathcal{F}_t$ is the information set available at time t. Thus, this may be interpreted as a very long-run forecast of the variable y_t which aligns directly with our survey data.

We use non-public data from the Federal Reserve Bank of New York's Survey of Primary Dealers (SPD). The SPD is conducted by the Trading Desk of the New York Fed one to two weeks before each regularly scheduled Federal Open Market Committee (FOMC) meeting and survey respondents are primary dealers (at the time of the survey) to the Federal Reserve Bank of New York.[1] Starting in July 2012, the survey began asking respondents about their "longer-run" forecasts for relevant economic variables. To our knowledge, the SPD is the only survey that explicitly solicits forecasts from private-sector respondents on "longer-run" values of economic variables.[2] This stands in contrast to a number of surveys which request farther in the future forecasts for economic variables with a specific horizon. The SPD collects longer-run forecasts of real GDP growth, the unemployment rate, the federal funds

[1] See https://www.newyorkfed.org/markets/primarydealer_survey_questions. Further information is available here: https://www.newyorkfed.org/markets/primarydealers.

[2] The Survey of Economic Projections (SEP), conducted by the FOMC, also reports longer-run values for these variables which is then mirrored by the SPD. In the SEP, "[l]onger-run projections represent each participant's assessment of the rate to which each variable would be expected to converge under appropriate monetary policy and in the absence of further shocks to the economy." See, for example, https://www.federalreserve.gov/monetarypolicy/files/fomcprojtabl20220921.pdf.

rate, and PCE inflation. We obtain an unbalanced panel of these forecasts for the entire available sample starting in mid-2012 which comprises 77 survey observations. Our sample includes 25 different primary dealers of which 16 primary dealers have forecasts for at least 70 of the 77 survey dates.[3]

Figure 1 presents the time series of different quantiles of the cross-sectional distribution of forecasts for real GDP growth, the unemployment rate, the federal funds rate, and the real federal funds rate. The latter is obtained by subtracting the longer-run PCE inflation forecast from the nominal federal funds rate forecast. First, there appears to be clear commonality in the movement of these longer-run forecasts with only modest disagreement across respondents. All four variables exhibit a downward trend over our sample period reflecting the perceived decline in potential output, the natural rate of unemployment, and the natural rate of interest (e.g., Crump, Eusepi, and Moench 2018, Holston, Laubach, and Williams 2017, Del Negro, Giannone, Giannoni, and Tambalotti 2018). Notably, the longer-run forecasts appear remarkably stable even after the onset of the COVID-19 pandemic.

Importantly, across all four variables, we can observe two key properties of these longer-run forecasts that will later serve to motivate our theoretical approach. First, the longer-run values of these economic variables are perceived to move over time but in a slow and deliberate fashion. Second, there are distinct periods of unchanged forecasts along with periods where forecasts change at a constant rate. This provides suggestive evidence that differences or second differences of forecasts for longer-run variables regularly take on values of zero.

We can demonstrate these properties by examining the empirical distribution of changes in longer-run forecasts. Figure 2 shows histograms of the first- and second-differences of longer-run forecasts from the SPD. Each chart presents two histograms. The first histogram pools all forecasts across survey respondents and time periods. The second histogram is an optimal aggregator of the histograms for each individual survey respondent. The weights are obtained by minimizing the Hellinger distance between the pooled histogram and the

[3]All of our empirical results are robust to excluding the 9 primary dealers who have shorter reporting periods.

optimal-weighted aggregator.[4] The most striking feature of Figure 2 is the disproportionate peak in each histogram at the bin centered at zero. This pattern holds across all variables and for both first and second differences.[5] Importantly, this behavior is driven by exact zero values rather than very small values. In particular, all four variables have between 80% and 85% of their first differences equal to zero and 66% to 74% of second differences equal to zero. As we move away from zero, we tend to observe a relatively wide but flat spread of observations. These histograms do not appear to be consistent with the behavior of a standard continuous distribution like the Gaussian distribution. Instead, the disparate behavior for small values relative to larger values (in magnitude) appears more consistent with a mixture distribution. This is precisely the methodological approach we undertake in the next section.

3 Sparse Trend Methodology

We begin with a description of the setup adopted throughout the paper. Suppose that we observe the time series $\{y_t\}_{t=1}^T$. We assume that y_t may be decomposed as

$$y_t = g_t + c_t, \qquad t = 1, \ldots, T, \tag{1}$$

for some "trend" g_t and corresponding deviation from trend c_t. Without further assumptions, we cannot make any progress in separating g_t from its deviation. To see this, note that we can set $\hat{g}_t = y_t$ and fit the data with no error. To avoid such an outcome, a popular class of estimators of the trend takes the form:

$$\min_{g_1,\ldots,g_T} \sum_{t=1}^{T} (y_t - g_t)^2 + \lambda_g \sum_{t=1}^{T} \ell\left(\Delta^k g_t\right), \tag{2}$$

[4] For more details and an application of this aggregation approach to asset-pricing models, see Gospodinov and Maasoumi (2021).

[5] In unreported results, we confirm that the same patterns hold at the individual forecaster level. These results are omitted to comply with data confidentiality restrictions of the SPD.

where Δ^k denotes the k-th order difference operator for $k \geq 1$ and $\ell(\cdot)$ is a penalty function with a penalty parameter λ_g. When $\ell(z) = z^2$ and $k = 2$, we obtain the HP filter (Hodrick and Prescott 1980). Similarly, for $\ell(z) = |z|$ and a fixed k, we obtain the trend filter of Tibshirani (2014).[6] Finally, when c_t is an independent white noise process, $\ell(z) = z^2$, and $k = 1$, then this is the Gaussian log-likelihood function of the local level model, where $\Delta g_t = v_t$ for some white noise process $\{v_t\}_{t=1}^T$. This latter case demonstrates clearly the direct link between the "nonparametric" formulation of the trend-estimation problem and the class of unobserved components models that is often cast in state-space form. In this example, the observation equation is equation (1) and the state equation is $g_t = g_{t-1} + v_t$, where equation (2) nests the log-likelihood function.[7]

To make further progress, we appeal to the common assumption of a "slow-moving" trend. This assumption is implemented, in practice, almost exclusively by modeling the trend component as non-stationary with a "small" innovation variance. Our approach, instead, aims to induce the desired low-frequency behavior through a prior which features sparsity in the changes in the estimated trend component as in the SPD data. As a convenient way to model the slow-moving trend and its associated estimation uncertainty, we develop our methods within a Bayesian framework. We impose sparsity by utilizing a spike-and-slab prior on the kth difference in the trend component, $\Delta^k g_t$. A spike-and-slab distribution is a mixture of one tightly concentrated density (the "spike") and a more diffuse density (the "slab") which weakens the link between small movements and large movements in the random variable. This accommodates slow-moving dynamics without compromising some occasional swiftness of movement in the series. In Appendix A.1, we provide further details and discuss the linkage with existing approaches.

Following a long tradition in economics, we assume that the deviation from trend (the "cycle") is serially correlated over time with degree of persistence determined by a parameter

[6] For a Bayesian approach to the trend filter, see Roualdes (2015).

[7] Grant and Chan (2017b) show that the HP filter can be obtained as the posterior mean of a Bayesian state-space model under the assumption of uncorrelated trend and white-noise cycle components, and the penalty parameter equal to the inverse of the signal-to-noise ratio.

vector γ. For parsimony, we assume that $c_t = y_t - g_t$ follows an $AR(\text{q})$ model[8]

$$c_t = \gamma_1 c_{t-1} + \cdots + \gamma_q c_{t-q} + \epsilon_t, \tag{3}$$

where $\gamma = (\gamma_1, \ldots, \gamma_q)'$. This approach for the cycle component leads to a more general form of equation (2),

$$\min_{\gamma, g_1, \ldots, g_T} \sum_{t=1}^{T} \epsilon_t^2 + \lambda_g \sum_{t=1}^{T} \ell\left(\Delta^k g_t\right) + \lambda_\gamma \sum_{i=1}^{q} |h_i(\gamma)|, \tag{4}$$

where $h_i(\gamma)$ represents a transformation of the autoregressive parameters and λ_γ is the associated penalty parameter. Two natural choices for $h_i(\cdot)$ are $h_i(\gamma) = \gamma_i$ and $h_i(\gamma) = \varphi_i$, where φ_i is the i-th partial autocorrelation coefficient. In what follows, we use $h_i(\gamma) = \gamma_i$.[9]

The solution to equation (4) and similar trend filters are presented as minimization problems that trade off model fit against a penalty term that induces smoothness on the trend estimates. However, they can also be interpreted, under certain conditions, as the posterior mode of the trend.[10] In our sparse trend filter, we build upon this Bayesian formulation, using spike-and-slab priors to induce sparsity. Our full prior setup is as follows.

We assume that the observed data $y = (y_1, \ldots, y_T)'$ satisfies

$$y \mid g, \gamma, \sigma^2 \sim \mathcal{N}(g, \sigma^2 \cdot \mathcal{V}_\gamma), \tag{5}$$

where $\mathcal{V}_\gamma$ denotes the variance-covariance matrix of a strictly stationary $AR(\text{q})$ process with unit innovation variance. We propose the following prior (and hyperprior) distributions on

[8]The focus here is on the low-frequency behavior of the observed process. Instead, if estimation of the cyclical component was the primary interest, then incorporating features such as outlier-augmented stochastic volatility may be appropriate (e.g., Stock and Watson 2016, Carriero, Clark, Marcellino, and Mertens 2022).

[9]The formulation using partial autocorrelation coefficients is omitted to conserve space and is available upon request from the authors. For regularization of partial autocorrelation coefficients when g_t is constant over time, see Schmidt and Makalic (2013).

[10]As an analogy, note that the LASSO estimator may be interpreted as the posterior mode when the regression coefficients have independent double exponential priors (Tibshirani 1996). In our setup, equation (4) gives the posterior mode for (g,γ) when independent double exponential priors are placed on the autoregressive coefficients, γ, and the kth differences of g_t. See Appendix A.1 for additional details.

the parameters. First, we assume that the trend, $g = (g_1, \ldots, g_T)'$, satisfies

$$g \mid \sigma^2, \omega, \gamma \sim \mathcal{N}(0, \sigma^2 \mathcal{V}_{\gamma,11} \cdot \Sigma_g), \qquad \Sigma_g^{-1} = D_k' \text{diag}(\omega_1, \ldots, \omega_{T-k})^{-1} D_k, \tag{6}$$

where $\mathcal{V}_{\gamma,11}$ is the $(1,1)$ element of $\mathcal{V}_\gamma$.[11] This additional factor ensures that our approach is scale invariant to y_t.[12] Here, D_k is the $(T-k) \times T$, k-difference matrix which maps a vector $(x_1, \ldots, x_T)'$ to $(\Delta^k x_{k+1}, \ldots, \Delta^k x_T)'$. The ω_j are the mixing variables for the Laplace distribution with mixing weights for g, $\{\omega_j : j = 1, \ldots, T-k\}$, which are conditionally independent with corresponding density

$$p\left(\omega_j \mid \lambda_g, \lambda_0, \theta_j\right) = (1-\theta_j)\frac{\lambda_0^2}{2}\exp\left\{\frac{-\lambda_0^2\omega_j}{2}\right\} + \theta_j\frac{\lambda_g^2}{2}\exp\left\{\frac{-\lambda_g^2\omega_j}{2}\right\}, \tag{7}$$

$$\theta_j \sim \text{Bernoulli}(\xi), \tag{8}$$

where λ_0 is fixed at a large number such that $\lambda_0 >> \lambda_g$ and θ_j is a dichotomous variable. This corresponds to the continuous spike-and-slab setup (see Ročková and George 2018), where θ_j can take on the value 0 (the "spike") or the value of 1 (the "slab"), governed by λ_g. The parameter λ_g governs the non-sparse movements in the prior of $\Delta^k g_t$ with larger values of λ_g corresponding to a tighter distribution around zero. The combination of equations (6)–(8) corresponds to the placement of a spike-and-slab prior on the kth difference of g_t.

Next, as is common in the literature (e.g., Park and Casella 2008), we place an uninformative prior on σ^2 as

$$p(\sigma^2) = 1/\sigma^2. \tag{9}$$

[11] The matrix Σ_g^{-1} is sparse. Drawing upon the insights from Chan and Jeliazkov (2009), Chan (2013), and Grant and Chan (2017a) we can exploit this sparsity for computational advantages. See the Appendix for full details.

[12] In some contexts, an alternative that does not scale Σ_g may be preferred (Moran, Ročková, and George 2019).

The common parameter ξ (see equation (8)) is distributed as,

$$\xi \sim \mathcal{B}\text{eta}(a, b). \tag{10}$$

Here, a and b are hyperparameters. In our implementation, we choose $a = b = 1$ which corresponds to a uniform prior.[13]

Finally, λ_g is distributed as $\lambda_g \sim \Gamma(r_g, \delta_g)$ with hyperparameters r_g and δ_g, where r_g is the *shape* parameter, and δ_g is the *rate* parameter. In principle, we could estimate λ_g via an empirical Bayes approach; however, we have found that a diffuse gamma prior gives similar posterior median estimates but is more computationally efficient and also allows us to accommodate the uncertainty from this parameter. Section SA.3 in the SA provides additional details about the distribution of λ_g.

For the cycle component, $c = (c_1, \ldots, c_T)'$ we assume that $c \sim \mathcal{N}(0, \sigma^2 \mathcal{V}_\gamma)$. Next, following a similar approach as for the trend, we impose

$$\gamma \mid \tau \sim \mathcal{N}(0, \Sigma_\gamma), \qquad \Sigma_\gamma = \text{diag}(\tau_1, \ldots, \tau_q), \tag{11}$$

and the mixing weights τ_j are conditionally independent for $j = 1, \ldots, q$ with density

$$p(\tau_j \mid \lambda_\gamma) = \frac{(\lambda_\gamma)_j^2}{2} \exp\left\{\frac{-(\lambda_\gamma)_j^2 \tau_j}{2}\right\}. \tag{12}$$

Finally, the additional penalty parameter λ_γ is distributed as,

$$\lambda_\gamma \sim \Gamma(r_\gamma, \delta_\gamma), \tag{13}$$

with hyperparameters r_γ and δ_γ, where r_γ is the shape parameter, and δ_γ is the rate parameter. In our empirical implementation, we choose r_γ and δ_γ that result in a relatively

[13] In some situations, one may want to place much more informative priors on ξ. Here, we choose an uninformative prior to be as conservative as possible to demonstrate that our results are not driven by the specific prior.

tight prior distribution for λ_γ around a small value. As we have discussed, our motivation is to have a cyclical component around a slow-moving trend which corresponds to little to no prior penalization on this term. To implement our Bayesian approach, we rely on a Gibbs sampling algorithm with a Metropolis-Hastings step for the cycle component. Appendix A.2 provides full operational details along with the choices for the hyperparameters. The proposed method can also be implemented when the cycle component is assumed to be white noise (see Section SA.1 in the SA).

4 Simulation Evidence

Before we move to the empirical applications, it is useful to assess the performance of our proposed procedure in a controlled environment. In this section, we demonstrate the benefits of our proposed procedure as compared to common alternatives in a series of simulation experiments. Even though our model is motivated by slow-moving trends, we explore different data generating processes to assess the performance of our estimator in more general settings. In the first design, we generate simulated data in levels to mimic the real GDP application in Section 5. This design is based on the unobserved components model of Morley, Nelson, and Zivot (2003) given by

$$
\begin{aligned}
y_t &= g_t + c_t, \\
g_t &= g_{t-1} + \mu + \epsilon_t^g, \qquad c_t = \gamma_1 c_{t-1} + \gamma_2 c_{t-2} + \epsilon_t.
\end{aligned}
$$

Here, $y_1 = 724.60$, $\mu = 0.81$, $(\gamma_1, \gamma_2) = (1.53, -0.61)$, and $\epsilon_t^g \sim_{i.i.d.} \mathcal{N}(0, 0.69^2)$ and $\epsilon_t \sim_{i.i.d.} \mathcal{N}(0, 0.62^2)$ and are mutually independent (see Table 1 in Morley, Nelson, and Zivot 2003). We refer to this data-generating process (DGP) as the "Level Model."

The remaining designs are meant to mimic the properties of data in growth rates. All of

the designs have the following general structure,

$$y_t = \mu + g_t + c_t,$$
$$g_t = g_{t-1} + \epsilon_t^g, \qquad c_t = \gamma_1 c_{t-1} + \sqrt{(1-\gamma_1^2)}\exp(h_t/2)\epsilon_t,$$

where $\mu = 3$, ϵ_t^g and ϵ_t are *i.i.d.* and mutually independent. We choose ϵ_t as either standard normal or chi-square with 3 degrees of freedom (centered and scaled to have mean zero and variance one). Under homoskedasticity, we set $h_t = 0\,\forall t$ and otherwise use the following stochastic volatility process: $h_t = 0.98h_{t-1} + \epsilon_t^h$, where $\epsilon_t^h \sim \mathcal{N}(0, 0.1^2)$ and is independent of all other variables. We use the designs featuring stochastic volatility and non-Gaussian errors to assess the sensitivity of all of the procedures to the presence of outliers and time-varying variances. Finally, we consider the following choices of ϵ_t^g:

- **Smooth Trend Model.** For this model, $\epsilon_t^g \sim \mathcal{N}(0, 0.06^2)$. This choice is based on the commonly-used "shifting endpoint" random walk trend (e.g., Stock and Watson 1989).

- **Small Structural Break Trend Model.** For this model, $\epsilon_t^g \sim \mathcal{N}(0, 0.05^2)$ with probability p_1 and $\epsilon_t^g \sim \mathcal{N}(0, 0.05^2 + 0.15^2)$ with probability $1 - p_1$. We set p_1 to 5% for a trend which features infrequent, modest in magnitude, and discontinuous moves.

- **Large Structural Break Trend Model.** Here, we set $\epsilon_t^g \sim \mathcal{N}(0, 0.8)$ with probability p_1 and $\epsilon_t^g \sim \mathcal{N}(0, 0.001^2)$ with probability $1 - p_1$. We set $p_1 = 0.02$ so that structural breaks are rare but likely to be dramatic when they occur. This design allows for sharper movements in the underlying trend – violating the "slow-moving" assumption – with a random timing and magnitude of the breakpoints.

We also consider a number of competing estimation procedures. The first alternative is the HP boosting procedure of Phillips and Shi (2020) which iterates the HP filter based on L2-boosting as a data-driven approach to adapt the degree of smoothness. We use a maximum of

100 iterations and an initial smoothing parameter of either 100, 1600 or 14400. In addition, we consider two wavelet-based estimators: the biorthogonal 17/11 wavelet filter used in Yogo (2008) and the reflected one-sided Haar wavelet filter of Lubik, Matthes, and Verona (2020) (see also Canova 2023). To implement our procedures, we follow the same approach as we do later in all of our empirical applications which is summarized in Appendices A.2.1 and SA.1 (in the SA). Here and throughout, we use the posterior median as our point estimate of the trend. For specifications with a serially correlated cycle component, we choose $q = 4$. Finally, all simulations are based on 1,000 Monte Carlo simulations with a sample size of $T = 250$.

To evaluate performance, we use the root mean-square error (RMSE) between the trend estimate and the true trend. In each table, we report the minimum and maximum of these metrics along with the mean and the 5th, 10th, 50th, 90th, and 95th percentiles of the realized RMSE across simulations.

Table 1 reports results for the level model. We only consider $k = 2$ in this case as the smooth (essentially) monotonic behavior of stock variables is inconsistent with recurrent periods of zero change. The RMSE values in the table and all other tables are reported as ratios relative to the benchmark of $k = 2$ with a serially correlated cycle. The benefit of including a cycle is demonstrated clearly in the first row when comparing to the case of $k = 2$ with a white noise cycle. As compared to HP boosting and the two wavelet approaches, we outperform in the vast majority of the cases with only slight underperformance in the worst case RMSE. We also make comparisons to the standard state-space model (the restricted model of Morley, Nelson, and Zivot 2003) which is correctly specified in this design. Our method outperforms the one-sided estimate uniformly but is dominated by the two-sided estimate, which is the MLE in this model, for about half of the simulations; however, the two-sided estimate can sometimes have very large RMSEs which our procedure avoids.

We next consider the smooth trend case which is the most common specification in the literature. Table 2 shows that our procedures for both $k = 1$ and $k = 2$ consistently out-

perform HP boosting and wavelets.[14] Even the closest competitor in this design – the Haar wavelet – exhibits an increase in RMSE of over 30%. Furthermore, allowing for stochastic volatility in the cycle component does not materially alter these conclusions.[15]

Table 3 presents results for the small structural break model. Again, we find that our method (both $k = 1$ and $k = 2$) dominates the competing alternatives. Perhaps unsurprisingly, the $k = 1$ estimator, which is better suited to the true trend process in this case, tends to perform best although its performance deteriorates under stochastic volatility and/or non-Gaussian innovations (see Table SA.2 in the SA). The robustness of the $k = 2$ estimator is clear from the table where the RMSEs of the alternative methods are higher by anywhere from 30% to well over 100%.

Finally, Table 4, presents results for the large break trend model with chi-square innovations to the cycle component. Because this design allows for sharp structural breaks in the trend, it is inherently disadvantageous to our procedures which are predicated on a slow-moving trend. However, Table 4 demonstrates the appealing robustness properties of our procedure with $k = 2$ as it still outperforms the competitors and reduces worst-case RMSE.

In the SA, we report additional simulation results for a number of different designs including the case where the true cycle is white noise. Importantly, we find that allowing for a serially-correlated cycle leads to very little deterioration in performance. This suggests that the cost of being more agnostic about the true DGP is relatively low. More generally, all of the simulation results in the SA are qualitatively similar to those presented in this section and underscore the appealing properties of our procedure. In sum, we find that our procedure performs well as compared to common alternatives for both $k = 1$ and $k = 2$. Between the two options, $k = 2$ may be preferred due to its demonstrated robustness properties. However, the procedure using $k = 1$ offers some advantages depending on the underlying nature of the

[14]Here and throughout, we always apply the HP boosting procedure to the level of the series and then, if necessary, translate to an estimate of the trend of the growth rate. We do so to ensure that the HP boosting procedure does not simply return the HP filter using the initialized smoothing parameter.

[15]To conserve space, we report the design with chi-square innovations to the cycle component in Table SA.1 of the SA.

process of interest.

5 Empirical Applications

We explore two main empirical applications. The first example considers the trend in the annual mean temperature change in the United States. The second application provides a comprehensive investigation of the underlying trend in real GDP and its components. In the SA, we present an additional empirical example studying the underlying trend in total factor productivity (TFP) growth.

5.1 Temperature Change in the United States

We first apply our estimator to data of the annual mean temperature change in the United States obtained from NASA, which cover the sample period 1880-2023.[16] The data are expressed as a deviation from the average temperature (in Celsius) over 1951–1980. Figure 3 presents these results. The top row shows the estimated underlying trend for both $k = 1$ and $k = 2$ using the approach introduced in Section 3. When $k = 1$, we observe that the underlying trend displays more pronounced local movements whereas for $k = 2$, the estimate is much smoother. Nevertheless, both trend estimates display a clear and strong upward trend since the mid-1970s. Each of the charts in the top row also show the estimated underlying trend under the assumption that the cycle is white noise. The similarity in the estimated trends, with and without a serially correlated cycle, highlights that the flexibility of a a serially correlated cycle does not appear to be costly in practice (as was also discussed in the previous section).

To assess the uncertainty around these estimates, the bottom left chart presents the estimated trend for $k = 2$ along with a 90% pointwise posterior coverage interval. We can observe that the estimated trend is precisely estimated. For example, the deviation from

[16] Data are available at https://data.giss.nasa.gov/gistemp/graphs_v4/.

the mean rose from 0.08 °C in 1979 (with 90% coverage interval of $[-0.06, 0.24]$) to 1.17 °C in 2023 (with 90% coverage interval of $[0.93, 1.41]$). We can draw even stronger conclusions by constructing uniform confidence bands as described by Olea and Plagborg-Møller (2019). To obtain the 90% uniform coverage interval, we construct a symmetric pointwise posterior coverage interval and increase the coverage rate until 90% of the posterior draws lay entirely within the band. The bottom right chart shows the corresponding uniform coverage interval. We first observe that it is much wider than its pointwise counterpart as would be expected. Second, and more importantly, we can clearly rule out that the current levels of the trend are consistent with the prevailing trend up to 1980. More specifically, no horizontal line (or monotonically decreasing function) resides entirely within the band, implying that the underlying trend has indeed shifted upward.

5.2 Real GDP Growth

As our main empirical application, we study the underlying trend in real GDP in the United States in the post-war era. The estimate of the unobserved trend component in real GDP growth, which is stripped of cyclical fluctuations, can inform policymakers of the long-run potential of the U.S. economy. The data is quarterly real GDP over the sample period of 1947:Q1–2023:Q4. We estimate the underlying trend in both the (log) level of real GDP and in its quarterly, annualized growth rate. As an additional exercise, we also construct a "bottom-up" estimate of the trend using the individual component contributions to real GDP growth.

We first estimate the trend in the log level of real GDP using $k = 2$ and $q = 4$ lags in the cycle component. Figure 4 presents the results from the estimation exercise. The left chart shows the log level of real GDP along with the estimated trend. Broadly speaking, we can observe that the trend is steeper in the first half of the sample than in the second half. Moreover, the trend flattened noticeably starting at around the Great Financial Crisis (GFC) in 2008. Finally, despite the substantial drop in real output during the pandemic,

the trend estimate does not appear to have been affected. In the right chart, we show the corresponding output gap estimate. We want to highlight a few additional noteworthy points. First, the output gap in the Great Recession does not appear to be unusually deep but it remains persistently negative for longer than any other post-war U.S. recession. The depth of the output gap in this episode is modulated by an appreciable estimated slowdown in trend growth in the 2000s with a strong positive output gap prior to the GFC. The output gap was closed by about mid-2019 before becoming deeply negative during the pandemic. As of 2023:Q4 the output gap appears to be essentially closed.

Based on the results shown in Figure 4, we can estimate trend real GDP growth which is also of key importance to policymakers. This is shown in the top left chart of Figure 5 along with 90% posterior coverage intervals against the backdrop of realized (annualized) real GDP growth.[17] As is well known, the first half of the sample period is characterized by more frequent recessions (denoted by the shaded areas) and higher output growth volatility. Despite this heterogeneous behavior, the estimated trend is smooth and slow-moving. The estimated trend has been declining over the sample and stands at 2.16% in the last quarter of 2023. This is lower than the CBO's estimate of potential growth (2.26% in 2023Q4) but above the median respondent from the SPD (1.9% in December 2023).

In the top right chart of Figure 5 we show the estimated trend when our procedure is applied directly to real GDP growth (rather than its level). We find a similar pattern in the estimated trend growth – broadly decreasing over the sample – but the degree of uncertainty is substantially larger especially at the endpoints. As such, we use the estimated trend obtained from the level of real GDP growth as our baseline. It is worthwhile to note that both of these trend estimates appear to be unaffected by the extreme volatility in real GDP observed during the pandemic.

For comparison, we consider several alternative approaches commonly used in the economic literature for decomposing economic series into trend and cycle. The workhorse models

[17]The y-axis has been truncated because of the extreme observations in real GDP growth that occurred during 2020.

for estimating the trend and the cyclical component are the unobserved components (UC) models. The closest UC model to our approach is the Bayesian UC (BUC) of Grant and Chan (2017b) which specifies a random walk trend in the growth rate of real GDP along with an additive ARMA cyclical component. The bottom left chart of Figure 5 presents our trend estimate along with that of Grant and Chan (2017b) with a choice of an $AR(2)$ cycle. Although the estimated trends broadly co-move, we can observe that the BUC trend estimate is more volatile and displays residual cyclical behavior, tending to achieve local minima in NBER recessions. This demonstrates the advantages of our sparse modeling framework which produces trend estimates that do not systematically co-vary with the cycle.

The literature has highlighted some fragilities in the estimation of UC models and, as a result, flexible trend estimation approaches may be preferred due to their ostensible robustness properties. We consider the same alternative trend estimation methods that we explored in the simulation experiments. In the bottom-left chart we present the trend estimate from the Haar wavelet which is based on moving averages with different windows (Lubik, Matthes, and Verona 2020). As with the BUC, this estimate exhibits residual cyclical behavior and more substantial volatility than our trend estimate.

By far, the most common technique for estimating low-frequency trends in economic time series is the HP filter (Hodrick and Prescott 1980). Recently, Phillips and Shi (2020) have refined the original HP filter to produce a data-driven implementation with desirable theoretical properties. In the bottom right chart of Figure 5, we present the estimated trend for the real GDP growth rate, based on an application of the original HP filter and the boosted HP filter. We apply these procedures to the level of log real GDP as is the standard approach in practice. We can see immediately that the estimated trend growth rate is far more volatile than that of our procedure. Moreover, the recession shading illuminates that the variability of the two trend estimates appear to be governed by the state of the business cycle. In particular, trend real GDP growth is adjudged to be at its local minimum around recessions throughout the sample. Furthermore, during the Great Recession, the

HP-boosted estimate of trend growth falls below zero which would have suggested far less slack in the economy. In contrast, our trend estimate does not exhibit any cyclical behavior which is more akin to an HP filter with a very large choice of the penalty parameter (see, for example, Coibion, Gorodnichenko, and Ulate 2018). Finally, we also include results based on the biorthogonal 17/11 wavelet filter (Yogo 2008). Similar to the HP filter, this approach also produces an estimate which is more variable and cyclical than our method.

There is a natural commonality in all of the approaches to low frequency estimation as they can accommodate different behavior with different choices for the tuning parameter. All of these approaches, for a specific choice of tuning parameter, would produce trend estimates that are similar to our method. However, it is important to emphasize that unlike these other methods, our tuning parameter selection is conducted in a data-driven way. Our procedure's ability to outperform alternative approaches by selecting the correct tuning parameter from the data is a significant advantage and obviates the need for "rules of thumb" based on the frequency of the data.

Although trend estimates of real output are relatively common in the literature, the underlying components generally receive scant attention. A bottom-up approach to trend estimation may reveal differential properties than using aggregate output as the target series. In Figure 6, we apply our methodology to the underlying contributions to real GDP growth from personal consumption expenditures, residential investment, business fixed investment, federal government expenditures, state and local government expenditures, net exports and the change in inventories.[18] The charts in Figure 6 show the realized series along with our trend estimate.

Several features of the data are worth noting. A few series display outsized volatility at the beginning of the sample, likely representing the transition into a post-war economy. The so-called Great Moderation – a decline in the variability in real GDP growth starting in the

[18] All series are available from https://fred.stlouisfed.org/: Real GDP (GDPC1); Personal Consumption Expenditures (DPCERY2Q224SBEA); Change in Inventories (A014RY2Q224SBEA); Residential Investment (A011RY2Q224SBEA); Business Fixed Investment (A008RY2Q224SBEA); Federal Government (A823RY2Q224SBEA); State & Local Government (A829RY2Q224SBEA); Net Exports (A019RY2Q224SBEA).

mid 1980s – is only reflected in the underlying behavior of a subset of series. In particular, residential investment, federal government expenditures, and the change in inventories exhibit pronounced reductions in volatility in the second half of the sample. Finally, the different sub-components of real GDP growth appear to display different serial correlation properties around a time-varying central tendency.

Figure 6 shows that across all of the components, we estimate relatively slow-moving trends. For example, the trend growth rate of personal consumption expenditures (which represents the dominant component of U.S. GDP) largely follows similar dynamics as for real GDP growth with a global peak in the mid-1960s at about 2.5% and a sharp drop from 2.3% in the late 1990s to a local trough of 1.3% in 2011 before recovering to about 2% at the end of the sample. Another notable series which exhibits interesting trend dynamics is the state and local government contribution to real GDP growth. Our estimates suggest that the trend growth has been broadly declining and fell to about zero in the aftermath of the Great Recession but has recovered steadily since then.

The underlying components of real GDP growth can be used as a pseudo "out-of-sample" metric to investigate the robustness properties of our approach. The underlying contributions display heterogeneous dynamics such as different volatility regimes, changes in persistence, and more pronounced non-Gaussian features. In this respect, we exploit the richness of the GDP data to assess the robustness properties of our trend estimation procedure.[19] The bottom right chart in Figure 6 compares the "top-down" and "bottom-up" trend estimates using our methodology. By "top-down" we refer to trend estimation based on aggregate real GDP growth as reported in Figure 5 and "bottom-up" refers to adding up the trend estimates of the sub-components. We can observe that there is essentially no difference between the two approaches with an average absolute deviation of 6 basis points.

[19] In Section SA.3 of the SA we also present evidence for the robustness of the trend estimate relative to the prior of λ_g.

6 Conclusion

Many variables of interest in economics and finance are obtained by decomposing observable processes into unobserved components. This is an innately challenging problem as assumptions are necessary to reliably separate the contributions from each component. In this paper, we adopt an approach motivated by the frequently used notion that the economic trend of interest is "slow-moving." Using novel survey data, we show that perceptions of slow-moving trends are characterized by sparse adjustments. This informs our Bayesian approach that combines spike-and-slab priors on changes in the underlying trend with a deviation from trend which is allowed to be serially correlated. We illustrate in simulations that our method performs well.

We apply our method in two empirical settings: mean temperature changes in the U.S. over the last 140 years, and post-war real GDP growth and its sub-components. In our climate application, we estimate a clearly upward underlying trend with an inflection point in the mid-1970s. Based on the trend estimates at the end of our sample, one would anticipate a rise in temperatures of between 0.2 and 0.3 °C over the next ten years. In our primary application, we estimate that trend real GDP growth in the U.S. has been falling since the 1960s and now stands slightly above 2%. While we show that trend estimates from other popular procedures appear to inherit some residual business cycle cyclicality, our method produces slow-moving trend estimates which do not systematically co-vary with the cycle.

Our method can be readily extended to a multivariate setting. The SPD data illustrate that longer-run forecasts appear to co-move across different economic variables, suggesting that they could be modeled jointly. Moreover, this could be beneficial as using external information or a multivariate model to impose economic restrictions (e.g., Phillips curve, Okun's law, etc.) is likely to sharpen identification and inference (e.g., see Müller, Stock, and Watson 2020). Our method is also applicable in settings – for example, impulse responses in local projection models – that may require flexible de-trending of the data prior to the analysis. These extensions are currently under investigation by the authors.

References

Baxter, M., and R. G. King (1999): "Measuring Business Cycles: Approximate Band-Pass Filters For Economic Time Series," *Review of Economics and Statistics*, 81(4), 575–593.

Beveridge, S., and C. Nelson (1981): "A New Approach to Decomposition of Economic Time Series into Permanent and Transitory Components with Particular Attention to Measurement of the 'Business Cycle'," *Journal of Monetary Economics*, 7(2), 151–174.

Canova, F. (2023): "FAQ: How Do I Measure the Output Gap?," Working paper.

Carriero, A., T. E. Clark, M. Marcellino, and E. Mertens (2022): "Addressing COVID-19 Outliers in BVARs with Stochastic Volatility," *Review of Economics and Statistics*, pp. 1–38.

Chan, J. C., and I. Jeliazkov (2009): "Efficient Simulation and Integrated Likelihood Estimation in State Space Models," *International Journal of Mathematical Modelling and Numerical Optimisation*, 1(1-2), 101–120.

Chan, J. C. C. (2013): "Moving Average Stochastic Volatility Models with Application to Inflation Forecast," *Journal of Econometrics*, 176(2), 162–172.

Coibion, O., Y. Gorodnichenko, and M. Ulate (2018): "The Cyclical Sensitivity in Estimates of Potential Output," *Brookings Papers on Economic Activity*, 49(2), 343–411.

Crump, R. K., S. Eusepi, M. Giannoni, and A. Şahin (2019): "A Unified Approach to Measuring u*," *Brookings Papers on Economic Activity*, 50(1), 143–214.

Crump, R. K., S. Eusepi, and E. Moench (2018): "The Term Structure of Expectations and Bond Yields," Staff Report 775, Federal Reserve Bank of New York.

Del Negro, M., D. Giannone, M. P. Giannoni, and A. Tambalotti (2018): "Safety, Liquidity, and the Natural Rate of Interest," *Brookings Papers on Economic Activity*, 49(1), 235–94.

——— (2019): "Global Trends in Interest Rates," *Journal of International Economics*, 118(1), 248–262.

Dufays, A., Z. Li, J. V. Rombouts, and Y. Song (2021): "Sparse Change-Point VAR Models," *Journal of Applied Econometrics*, 36, 703–727.

Dufays, A., and J. V. Rombouts (2020): "Relevant Parameter Changes in Structural Break Models," *Journal of Econometrics*, 217(1), 46–78.

Eo, Y., and J. Morley (2022): "Why Has the U.S. Economy Stagnated Since the Great Recession?," *The Review of Economics and Statistics*, 104(2), 246–258.

Fernald, J. G., R. E. Hall, J. H. Stock, and M. W. Watson (2017): "The Disappointing Recovery of Output after 2009," *Brookings Papers on Economic Activity*, 48(2).

Florian Huber, G. K., and L. Onorante (2021): "Inducing Sparsity and Shrinkage in Time-Varying Parameter Models," *Journal of Business & Economic Statistics*, 39(3), 669–683.

Gospodinov, N., and E. Maasoumi (2021): "Generalized Aggregation of Misspecified Models: With an Application to Asset Pricing," *Journal of Econometrics*, 222(1(B)), 451–467.

Grant, A. L., and J. C. Chan (2017a): "A Bayesian Model Comparison for Trend-Cycle Decompositions of Output," *Journal of Money, Credit and Banking*, 49(2-3), 525–552.

——— (2017b): "Reconciling Output Gaps: Unobserved Components Model and Hodrick-Prescott filter," *Journal of Economic Dynamics and Control*, 75(1), 114–121.

Hamilton, J. D. (2018): "Why You Should Never Use the Hodrick-Prescott Filter," *Review of Economics and Statistics*, 100(5), 831–843.

Harvey, A. C., T. M. Trimbur, and H. K. Van Dijk (2007): "Trends and Cycles in Economic Time Series: A Bayesian Approach," *Journal of Econometrics*, 140(2), 618–649.

Hodrick, R. J. (2020): "An Exploration of Trend-Cycle Decomposition Methodologies in Simulated Data," Working Paper 26750, National Bureau of Economic Research.

Hodrick, R. J., and E. C. Prescott (1980): "Postwar US Business Cycles: An Empirical Investigation," Discussion paper, Carnegie-Mellon University.

Holston, K., T. Laubach, and J. C. Williams (2017): "Measuring the Natural Rate of Interest: International Trends and Determinants," *Journal of International Economics*, 108(1), S59–S75.

Kamber, G., J. Morley, and B. Wong (2018): "Intuitive and Reliable Estimates of the Output Gap from a Beveridge-Nelson Filter," *Review of Economics and Statistics*, 100(3), 550–566.

Kim, S.-J., K. Koh, S. Boyd, and D. Gorinevsky (2009): "L1 Trend Filtering," *SIAM Review*, 51(2), 339–360.

Koop, G., and S. M. Potter (2007): "Estimation and Forecasting in Models with Multiple Breaks," *Review of Economic Studies*, 74(3), 763–789.

Laubach, T., and J. C. Williams (2003): "Measuring the Natural Rate of Interest," *Review of Economics and Statistics*, 85(4), 1063–1070.

Lee, S., Y. Liao, M. H. Seo, and Y. Shin (2021): "Sparse HP Filter: Finding Kinks in the COVID-19 Contact Rate," *Journal of Econometrics*, 220(1), 158–180.

Lubik, T., C. Matthes, and F. Verona (2020): "Assessing U.S. Aggregate Fluctuations Across Time and Frequencies," Working paper.

Moran, G. E., V. Ročková, and E. I. George (2019): "Variance Prior Forms for High-Dimensional Bayesian Variable Selection," *Bayesian Analysis*, 14(4), 1091–1119.

Morley, J. C., C. R. Nelson, and E. Zivot (2003): "Why Are the Beveridge-Nelson and Unobserved-Components Decompositions of GDP so Different?," *Review of Economics and Statistics*, 85(2), 235–243.

Müller, U. K., J. H. Stock, and M. W. Watson (2020): "An Econometric Model of International Growth Dynamics for Long-horizon Forecasting," *Review of Economics and Statistics*, forthcoming.

Olea, J. L. M., and M. Plagborg-Møller (2019): "Simultaneous Confidence Bands: Theory, Implementation, and an Application to SVARs," *Journal of Applied Econometrics*, 34(1), 1–17.

Park, T., and G. Casella (2008): "The Bayesian LASSO," *Journal of the American Statistical Association*, 103(482), 681–686.

Phillips, P. C. B., and Z. Shi (2020): "Boosting: Why You Can Use the HP Filter," *International Economic Review*, forthcoming.

Prüser, J. (2021): "The Horseshoe Prior for Time-Varying Parameter VARs and Monetary Policy," *Journal of Economic Dynamics and Control*, 129, Article 104188.

Roualdes, E. A. (2015): "Bayesian Trend Filtering," Working paper.

Ročková, V., and E. I. George (2018): "The Spike-and-Slab LASSO," *Journal of the American Statistical Association*, 113(521), 431–444.

Schmidt, D. F., and E. Makalic (2013): "Estimation of Stationary Autoregressive Models with the Bayesian LASSO," *Journal of Time Series Analysis*, 34, 517–531.

Stock, J. H., and M. W. Watson (1989): "New Indexes of Coincident and Leading Economic Indicators," in *NBER Macroeconomics Annual 1989*, vol. 4, pp. 351–409. National Bureau of Economic Research.

——— (2016): "Dynamic Factor Models, Factor-Augmented Vector Autoregressions, and Structural Vector Autoregressions in Macroeconomics," in *Handbook of Macroeconomics*, ed. by J. B. Taylor, and H. Uhlig, vol. 2A, chap. 8, pp. 415–525. Elsevier.

Tibshirani, R. (1996): "Regression Shrinkage and Selection via the Lasso," *Journal of the Royal Statistical Society*, 58(1), 267–288.

Tibshirani, R. J. (2014): "Adaptive Piecewise Polynomial Estimation Via Trend Filtering," *Annals of Statistics*, 42(1), 285–323.

Yogo, M. (2008): "Measuring business cycles: A Wavelet Analysis of Economic Time Series," *Economics Letters*, 100(2), 208–212.

Appendix

A.1 Discussion of Slab and Spike Prior

In the frequentist case, a popular way to induce sparsity is to cast the estimator as a solution to a generalized LASSO problem. From a Bayesian perspective, the trend filter can be motivated following Park and Casella (2008). Park and Casella (2008) study the standard linear regression setting, where $Y|\, X, \beta, \sigma^2 \sim \mathcal{N}(X\beta, \sigma^2 I_T)$ and

$$p(\beta_1, \ldots, \beta_p|\sigma^2) = \prod_{j=1}^{p} \frac{1}{2\sqrt{\sigma^2}} \exp\left\{-\lambda \frac{|\beta_j|}{\sqrt{\sigma^2}}\right\}. \tag{A.1}$$

In its hierarchical form,[20]

$$\beta_1, \ldots, \beta_p \left| \sigma^2, \varkappa_1, \ldots, \varkappa_p \sim \mathcal{N}\left(0, \sigma^2 \cdot \text{diag}\left(\varkappa_1, \ldots, \varkappa_p\right)\right), \right. \tag{A.2}$$

$$p\left(\varkappa_1, \ldots, \varkappa_p \middle| \sigma^2, \lambda\right) = \prod_{i=1}^{p} \left(\frac{\lambda^2}{2}\right) \exp\left\{\frac{-\lambda^2 \varkappa_i}{2}\right\} \tag{A.3}$$

with $p(\sigma^2) = 1/\sigma^2$.

The Bayesian trend filter can then be obtained setting $p = T$, $X = I_T$, $\beta_t = g_t$ and the priors applied to each of the $\Delta^k g_t$ (Roualdes 2015). We instead utilize a spike-and-slab prior which weakens the link between small and large movements in the random variable. It is instructive to compare the prior assumptions underpinning the Bayesian LASSO above to our spike-and-slab formulation. In the Bayesian LASSO, sampling is performed from a single Laplace density. In contrast, Figure A.1 provides an example of the two Laplace densities that comprise the continuous spike-and-slab setup.[21] The solid line represents the "spike" and the dashed line represents the "slab". We observe clear similarities in the implied mixture distribution of Figure A.1 and the survey data presented in Figure 2.

Although our focus is on the "slow-moving" trend assumption, there is a closely related literature that endeavors to impose sparsity but with the allowance of much larger, occasional movements – primarily with respect to time-varying parameter models. Two notable strands of this literature are Bayesian change point models (e.g., Koop and Potter 2007, Dufays and Rombouts 2020, and Dufays, Li, Rombouts, and Song 2021) and Bayesian shrinkage for time-varying parameters (e.g., Florian Huber and Onorante 2021 or Prüser 2021). While this literature is related to our approach, these procedures are motivated by different assumptions, and so we do not consider them further in this paper.

[20] The hierarchical form uses the representation of the Laplace distribution as a scale mixture of normals (with an exponential mixing density). See Park and Casella (2008) for further discussion.

[21] In practice, when we implement the spike-and-slab formulation, the difference between the two densities is even more extreme but we reduce the differences in Figure A.1 for presentation purposes.

Figure A.1: **Spike and Slab Densities.** This figure illustrates the role of the two densities in the continuous spike and slab setup.

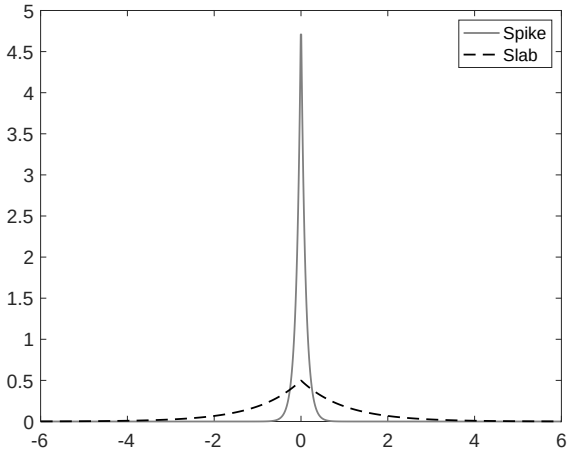

A.2 Description of Gibbs Sampling Algorithm

This Appendix details the implementation of the estimation procedure introduced in Section 3. Section A.2.1 provides the steps for the Gibbs sampler whereas further details underlying each individual step are given in Appendix A.2.2. Finally, Section SA.1 in the Supplemental Appendix provides steps for the case of a white-noise cycle.

A.2.1 Implementation Steps

Throughout, we use the same notation as in Section 3. In addition, define $S := \sum_{j=1}^{T-k} \theta_j$. For convenience, we partition the density of the cycle component, $c = (c_1, \ldots, c_T)'$, as

$$p(\, c|\, \gamma, \sigma^2) = p\big(c_{q+1:T} \mid c_{1:q}, \gamma, \sigma^2\big) p\big(c_{1:q} \mid \gamma, \sigma^2\big), \tag{A.4}$$

where $c_{1:q}$ are the first q observations of c_t, $c_{q+1:T}$ are the last $T-q$ observations, and

$$p\big(c_{q+1:T} \mid c_{1:q}, \gamma, \sigma^2\big) \propto \frac{1}{\sigma^{(T-q)}} \exp\left\{-\frac{(c - B_{c,q}\gamma)'(c - B_{c,q}\gamma)}{2\sigma^2}\right\} \tag{A.5}$$

with $B_{c,q}$ denoting a $(T-q)\times q$ matrix with i-th row equal to $(c_{i+q-1}, c_{i+q-2}\ldots, c_i)$. For the initial conditions, we have

$$p\big(c_{1:q} \mid \gamma, \sigma^2\big) \propto \frac{1}{\det(\sigma^2 \mathcal{V}_\gamma)^{1/2}} \exp\left\{-\frac{c_{1:q}' \mathcal{V}_\gamma^{-1} c_{1:q}}{2\sigma^2}\right\}. \tag{A.6}$$

In addition, define $v_{sc}(\gamma) = \sigma^2 \cdot \mathcal{V}_{\gamma,11}$. Note that the Metropolis-Hastings step (Step 8 below) is required to draw γ in the Gibbs sampler because (i) we assume a strictly stationary autoregressive process and (ii) the prior variance of the trend g is a function of $\mathcal{V}_\gamma$. However, we follow the approach of Del Negro, Giannone, Giannoni, and Tambalotti (2019), tailored to our setting, and use the conditional distribution of the LASSO estimator (conditional on the q initial conditions of $c = y - g$) as our candidate distribution. This results in a simple accept-reject rule which performs well in practice. Consequently, our Gibbs sampler remains computationally efficient with standard software implementation.[22] The steps of the Gibbs sampler are as follows:

1. Draw $(\lambda_g \mid g, \gamma, \sigma^2, \theta, r_g, \delta_g) \sim \Gamma\left(S + r_g,\ \delta_g + \sum_{j=1}^{T-k} \frac{\theta_j |(D_k g)_j|}{\sqrt{v_{sc}(\gamma)}}\right)$.

2. Draw $(\sigma^2 \mid y, g, \gamma) \sim \textsc{Inverse-Gamma}\left(T - \frac{k}{2},\ \frac{1}{2}\left((y-g)'\mathcal{V}_\gamma^{-1}(y-g) + \frac{1}{\mathcal{V}_{\gamma,11}} g'\Sigma_g^{-1} g\right)\right)$.

3. Draw $(\xi \mid \theta) \sim \mathcal{B}eta(S + a, T - k - S + b)$.

4. Draw each $(\theta_j \mid g, \gamma, \sigma^2, \lambda_g, \lambda_0, \xi)$ as an independent Bernoulli random variable with

$$P(\theta_j = 0) = \frac{(1-\xi)\lambda_0 e^{-\sqrt{\lambda_0^2 (D_k g)_j^2 / v_{sc}(\gamma)}}}{(1-\xi)\lambda_0 e^{-\sqrt{\lambda_0^2 (D_k g)_j^2 / v_{sc}(\gamma)}} + \xi \lambda_g e^{-\sqrt{\lambda_g^2 (D_k g)_j^2 / v_{sc}(\gamma)}}},$$

$$P(\theta_j = 1) = \frac{\xi \lambda_g e^{-\sqrt{\lambda_g^2 (D_k g)_j^2 / v_{sc}(\gamma)}}}{(1-\xi)\lambda_0 e^{-\sqrt{\lambda_0^2 (D_k g)_j^2 / v_{sc}(\gamma)}} + \xi \lambda_g e^{-\sqrt{\lambda_g^2 (D_k g)_j^2 / v_{sc}(\gamma)}}},$$

for $j = 1, \ldots, T-k$.

[22] In our simulations and empirical exercises, we use `MATLAB` to implement our procedure. As a reference, the estimation of the trend in real GDP ($T = 308$) takes less than 35 seconds based on 100,000 posterior draws, 50,000 of which we discard as burn-in draws.

5. Draw each $(\frac{1}{\omega_j} \mid g, \gamma, \theta_j, \lambda_g) \sim$ INVERSE-GAUSSIAN $\left(\sqrt{\frac{\left((1-\theta_j)\lambda_0^2 + \theta_j \lambda_g^2\right) v_{sc}(\gamma)}{|(D_k g)_j|^2}},\ (1-\theta_j)\lambda_0^2 + \theta_j \lambda_g^2 \right)$ independently for $j = 1, \ldots, T-k$.

6. Draw $(g \mid y, \sigma^2, \gamma, \omega) \sim \mathcal{N}\left(\left(\mathcal{V}_\gamma^{-1} + \frac{\sigma^2}{v_{sc}(\gamma)} \Sigma_g^{-1} \right)^{-1} \mathcal{V}_\gamma^{-1} y,\ \sigma^2 \left(\mathcal{V}_\gamma^{-1} + \frac{\sigma^2}{v_{sc}(\gamma)} \Sigma_g^{-1} \right)^{-1} \right)$. See Remark 1 below.

7. Draw $(\lambda_\gamma \mid \gamma, r_\gamma, \delta_\gamma) \sim \Gamma\left(q + r_\gamma,\ \delta_\gamma + \sum_{j=1}^q |\gamma_j| \right)$.

8. Given the values in Steps 1–7, jointly draw (γ, Σ_γ) through the following steps:

   (a) Draw each $(\frac{1}{\tau_j^o}) \sim$ INVERSE-GAUSSIAN $\left(\left| \frac{\lambda_\gamma}{\gamma_j} \right|,\ \lambda_\gamma^2 \right)$ independently for $j = 1, \ldots, q$. Set $\Sigma_\gamma^o = \text{diag}(\tau_1^o, \ldots, \tau_q^o)$.

   (b) Draw $\gamma^o \sim \mathcal{N}\left(C B_{c,q}' c_{q+1:T},\ \sigma^2 C \right)$, where $C = (B_{c,q}' B_{c,q} + \sigma^2 \left(\Sigma_\gamma^o\right)^{-1})^{-1}$ and $c_{q+1:T}$ is the vector comprised of the last $T-q$ elements of c.

   (c) Let $\gamma^{(t)}$ denote the previous Gibbs draw of γ. If γ^o implies a stationary cycle component, set $(\gamma, \Sigma_\gamma) = (\gamma^o, \Sigma_\gamma^o)$ with probability

$$\min\left\{ \left(\frac{(\mathcal{V}_{\gamma^{(t)},11})^{T-k} |\mathcal{V}_{\gamma^{(t)}}|}{(\mathcal{V}_{\gamma^o,11})^{T-k} |\mathcal{V}_{\gamma^o}|} \right)^{1/2} \exp\left\{ \frac{c_{1:q}' \left(\mathcal{V}_{\gamma^{(t)}}^{-1} - \mathcal{V}_{\gamma^o}^{-1} \right) c_{1:q}}{2\sigma^2} + \frac{g' \Sigma_g^{-1} g}{2\sigma^2} \left(\frac{1}{\mathcal{V}_{\gamma^{(t)},11}} - \frac{1}{\mathcal{V}_{\gamma^o,11}} \right) \right\},\ 1 \right\}$$

   and set $(\gamma, \Sigma_\gamma) = \left(\gamma^{(t)}, \Sigma_\gamma^{(t)} \right)$ otherwise.

In our empirical implementations, we choose $\lambda_0 = 100$, $(r_g, \delta_g) = (2.5, 0.25)$ for $k = 1$, and $\lambda_0 = 4{,}000$, $(r_g, \delta_g) = (2.25, 0.0075)$ for $k = 2$. We also choose $(r_\gamma, \delta_\gamma) = (0.5, 0.25)$. The empirical applications (simulation exercises) are based on 100,000 (40,000) posterior draws, 50,000 (20,000) of which we discard as burn-in draws.

Remark 1. In Step 6, we follow Chan and Jeliazkov (2009), Chan (2013), and Grant and Chan (2017a). We define all banded matrices as sparse matrices (using the `speye`, `spdiags`, and `sparse` commands in `MATLAB`). We need to draw, $(g \mid y, \sigma^2, \gamma, \omega) \sim \mathcal{N}\left(\mathcal{B}^{-1} \mathcal{V}_\gamma^{-1} y,\ \sigma^2 \mathcal{B}^{-1} \right)$,

where $\mathcal{B} = \mathcal{V}_\gamma^{-1} + \frac{\sigma^2}{v_{sc}(\gamma)}\Sigma_g^{-1}$. To do so, we obtain the Cholesky factor $\mathcal{C}$ of $\mathcal{B}$, convert the banded $\mathcal{C}$ matrix into a sparse matrix, and solve $\mathcal{C}'\mathcal{C}\mu = \mathcal{V}_\gamma^{-1}y$ for the conditional mean μ (using `C\(C'\B)` in `MATLAB`). After drawing u from the standard normal distribution and solving $\mathcal{C}\tilde{g} = u$, we obtain $g = \mu + \sigma\tilde{g}$ that follows the desired distribution. □

A.2.2 Details of Gibbs Sampler Steps

In this section, we provide some additional detail on the derivation of the Gibbs sampler for the trend plus cycle specification introduced in the previous section. The results apply readily to the simpler trend plus noise specification given in the SA.

Steps 1–3 of Appendix A.2.1

Drawing λ_g: In the paper, we utilize the representation of the Laplace distribution as a scale mixture of normals with an exponential mixing density as in Park and Casella (2008) (i.e., equations (6) and (7)). We may write the conditional density of $(D_k g)_i$ directly as

$$p\big((D_k g)_i \mid \gamma, \sigma^2, \theta_i, \lambda_g, \lambda_0\big) = (1-\theta_j)\frac{\lambda_0}{2\sqrt{v_{sc}(\gamma)}}\exp\left\{-\lambda_0\frac{|(D_k g)_i|}{\sqrt{v_{sc}(\gamma)}}\right\} + \theta_j\frac{\lambda_g}{2\sqrt{v_{sc}(\gamma)}}\exp\left\{-\lambda_g\frac{|(D_k g)_i|}{\sqrt{v_{sc}(\gamma)}}\right\}.$$

The conditional distribution of λ_g is then

$$\begin{aligned} p\left(\lambda_g \mid g, \gamma, \sigma^2, \theta, r_g, \delta_g\right) &\propto p\left(g \mid \gamma, \sigma^2, \lambda_g, \theta, r_g, \delta_g\right) \cdot p\left(\lambda_g \mid r_g, \delta_g\right) \\ &\propto \left(\prod_{j|\theta_j=1} \frac{\lambda_g}{2\sqrt{v_{sc}(\gamma)}}\exp\left\{-\lambda_g\frac{|(D_k g)_j|}{\sqrt{v_{sc}(\gamma)}}\right\}\right) \cdot (\lambda_g)^{r_g-1}\exp\{-\delta_g\lambda_g\}. \end{aligned}$$

Thus, as in Step 1, we have $(\lambda_g \mid g, \gamma, \sigma^2, \theta, r_g, \delta_g) \sim \Gamma\left(S + r_g,\ \delta_g + \sum \frac{\theta_j|(D_k g)_j|}{\sqrt{v_{sc}(\gamma)}}\right)$.

Drawing σ^2: Using the joint density and the prior for σ^2 in equation (9), we obtain

$$p(y, g, \omega, \lambda_g, \gamma, \tau, \lambda_\gamma, \sigma^2) \propto \frac{1}{\sigma^T}\exp\left\{-\frac{(y-g)'\mathcal{V}_\gamma^{-1}(y-g)}{2\sigma^2}\right\}\frac{1}{\sigma^{T-k}}\exp\left\{-\frac{g'\Sigma_g^{-1}g}{2v_{sc}(\gamma)}\right\}\frac{1}{\sigma^2}$$

$$\propto \frac{1}{\sigma^{2T+2-k}} \exp\left\{-\frac{(y-g)'\mathcal{V}_\gamma^{-1}(y-g) + \frac{1}{\mathcal{V}_{\gamma,11}} g'\Sigma_g^{-1} g}{2\sigma^2}\right\}.$$

Thus, as in Step 2, we obtain

$$\left(\sigma^2 \mid y, g, \gamma\right) \sim \textsc{Inverse-Gamma}\left(T - \frac{k}{2},\ \frac{1}{2}\left((y-g)'\mathcal{V}_\gamma^{-1}(y-g) + \frac{1}{\mathcal{V}_{\gamma,11}} g'\Sigma_g^{-1} g\right)\right).$$

Drawing ξ : Using the priors introduced in equations (8) and (10) we obtain,

$$p(\xi \mid \theta, a, b) \propto p(\theta \mid \xi) \cdot p(\xi \mid a, b) \propto (1-\xi)^{T-k-S+b-1} \xi^{S+a-1}.$$

Thus, as in Step 3, we obtain $(\xi \mid \theta, a, b) \sim \mathcal{B}eta(S+a,\ T-k-S+b)$.

Steps 4–5 of Appendix A.2.1

Our method for sampling from the joint distribution of ω_j and θ_j is to first sample θ_j from its marginal distribution and then sample ω_j from its corresponding conditional distribution. We first derive the joint distribution of ω_j and θ_j:

$$\begin{aligned} p(\omega_j, \theta_j \mid g, \gamma, \sigma^2, \lambda_g, \lambda_0, \xi) &\propto p(g \mid \omega_j, \theta_j, \gamma, \sigma^2) \cdot p(\omega_j \mid \lambda_g, \lambda_0, \theta_j) \cdot p(\theta_j \mid \xi) \\ &\propto \left((1-\theta_j)(1-\xi)\frac{\lambda_0^2}{2}\exp\left\{\frac{-\lambda_0^2\omega_j}{2}\right\} + \theta_j\xi\frac{\lambda_g^2}{2}\exp\left\{\frac{-\lambda_g^2\omega_j}{2}\right\}\right) \\ &\quad \times \frac{1}{\omega_j^{1/2}} \exp\left\{-\frac{\omega_j^{-1}(D_k g)_j^2}{2v_{sc}(\gamma)}\right\}. \end{aligned}$$

This last equation can be rewritten as:

$$\begin{aligned} p(\omega_j, \theta_j \mid g, \gamma, \sigma^2, \lambda_g, \lambda_0, \xi) \propto (1-\theta_j)\frac{(1-\xi)\lambda_0^2}{\omega_j^{1/2}} \exp\left\{-\frac{\omega_j^{-1}(D_k g)_j^2}{2v_{sc}(\gamma)} - \frac{\lambda_0^2\omega_j}{2}\right\} \\ + \theta_j \frac{\xi\lambda_g^2}{\omega_j^{1/2}} \exp\left\{-\frac{\omega_j^{-1}(D_k g)_j^2}{2v_{sc}(\gamma)} - \frac{\lambda_g^2\omega_j}{2}\right\}. \end{aligned} \tag{A.7}$$

Drawing θ_j : We further rewrite equation (A.7) as

$$p(\omega_j, \theta_j \mid g, \gamma, \sigma^2, \lambda_g, \lambda_0, \xi) \propto (1-\theta_j)\frac{\mathcal{C}_0}{\omega_j^{1/2}} \exp\left\{-\mathcal{A}\omega_j^{-1} - \mathcal{B}_0\omega_j\right\} + \theta_j \frac{\mathcal{C}_1}{\omega_j^{1/2}} \exp\left\{-\mathcal{A}\omega_j^{-1} - \mathcal{B}_1\omega_j\right\}$$

with $\mathcal{A} = \frac{(D_k g)_j^2}{2v_{sc}(\gamma)}$, $\mathcal{B}_0 = \frac{\lambda_0^2}{2}$, $\mathcal{B}_1 = \frac{\lambda_g^2}{2}$, $\mathcal{C}_0 = (1-\xi)\lambda_0^2$, $\mathcal{C}_1 = \xi\lambda_g^2$. We now can integrate over ω_j to get the marginal distribution of θ_j

$$\begin{aligned}
&p(\theta_j \mid g, \gamma, \sigma^2, \lambda_g, \lambda_0, \xi) \\
&= \int_0^\infty p(\omega_j, \theta_j \mid g, \gamma, \sigma^2, \lambda_g, \lambda_0, \xi)\ d\omega_j \\
&\propto \int_0^\infty \left[(1-\theta_j)\frac{\mathcal{C}_0}{\omega_j^{1/2}} \exp\left\{-\mathcal{A}\omega_j^{-1} - \mathcal{B}_0\omega_j\right\} + \theta_j \frac{\mathcal{C}_1}{\omega_j^{1/2}} \exp\left\{-\mathcal{A}\omega_j^{-1} - \mathcal{B}_1\omega_j\right\}\right] d\omega_j \\
&\propto (1-\theta_j)(1-\xi)\lambda_0 e^{-\sqrt{\lambda_0^2 (D_k g)_j^2 / v_{sc}(\gamma)}} + \theta_j \xi \lambda_g e^{-\sqrt{\lambda_g^2 (D_k g)_j^2 / v_{sc}(\gamma)}}.
\end{aligned}$$

The last step follows since the antiderivative of

$$\int_0^\infty \frac{\mathcal{C}}{\omega_j^{1/2}} \exp\left\{-\frac{\mathcal{A}}{\omega_j} - \mathcal{B}\omega_j\right\}\ d\omega_j$$

is

$$\frac{\mathcal{C}\sqrt{\pi}}{2\sqrt{\mathcal{B}}}\left(e^{2\sqrt{\mathcal{A}\mathcal{B}}}\text{erf}\left(\frac{\sqrt{\mathcal{A}} + \sqrt{\mathcal{B}}\omega_j}{\sqrt{\omega_j}}\right) - e^{-2\sqrt{\mathcal{A}\mathcal{B}}}\text{erf}\left(\frac{\sqrt{\mathcal{A}} - \sqrt{\mathcal{B}}\omega_j}{\sqrt{\omega_j}}\right)\right),$$

where $\text{erf}(x) = \frac{2}{\sqrt{\pi}}\int_0^x e^{-t^2}\ dt$. Consequently,

$$\int_0^\infty \frac{\mathcal{C}}{\omega_j^{1/2}} \exp\left\{-\frac{\mathcal{A}}{\omega_j} - \mathcal{B}\omega_j\right\}\ d\omega_j = \frac{\mathcal{C}\sqrt{\pi}}{\sqrt{\mathcal{B}}} e^{-2\sqrt{\mathcal{A}\mathcal{B}}}.$$

Thus, θ_j is a Bernoulli Random variable with

$$P(\theta_j = 1) = \frac{\xi\lambda_g e^{-\sqrt{\lambda_g^2 (D_k g)_j^2 / v_{sc}(\gamma)}}}{(1-\xi)\lambda_0 e^{-\sqrt{\lambda_0^2 (D_k g)_j^2 / v_{sc}(\gamma)}} + \xi\lambda_g e^{-\sqrt{\lambda_g^2 (D_k g)_j^2 / v_{sc}(\gamma)}}}.$$

Drawing ω_j : We now derive the conditional distribution of ω_j given θ_j:

$$
\begin{aligned}
&p(\omega_j \mid g, \gamma, \sigma^2, \lambda_g, \lambda_0, \theta_j) \\
&\propto p(g \mid \omega_j, \gamma, \sigma^2) \cdot p(\omega_j \mid \lambda_g, \lambda_0, \theta_j) \\
&\propto \frac{1}{|\Sigma_g|^{1/2}} \exp\left\{-\frac{g'\Sigma_g^{-1}g}{2v_{sc}(\gamma)}\right\} \left((1-\theta_j)\frac{\lambda_0^2}{2}\exp\left\{\frac{-\lambda_0^2\omega_j}{2}\right\} + \theta_j\frac{\lambda_g^2}{2}\exp\left\{\frac{-\lambda_g^2\omega_j}{2}\right\}\right) \\
&\propto \frac{1}{|\Sigma_g|^{1/2}} \exp\left\{-\frac{(D_k g)'\mathrm{diag}(\omega_1,\ldots,\omega_{T-k})D_k g}{2v_{sc}(\gamma)}\right\} \exp\left\{\frac{-\big((1-\theta_j)\lambda_0^2+\theta_j\lambda_g^2\big)\omega_j}{2}\right\}.
\end{aligned}
$$

The last step follows because θ_j only takes on the values of 0 or 1; in particular, only for these two values will the last two lines be proportional as a function of ω_j (their quotient is independent of ω_j, but dependent upon θ_j and λ_0, λ_g). Thus,

$$
p(\omega_j \mid g, \gamma, \sigma^2, \lambda_g, \lambda_0, \theta_j) \propto \frac{1}{\omega_j^{1/2}} \exp\left\{-\frac{\sum_{i=1}^{T-k}\omega_i^{-1}(D_k g)_i^2}{2v_{sc}(\gamma)}\right\} \exp\left\{\frac{-\big((1-\theta_j)\lambda_0^2+\theta_j\lambda_g^2\big)\omega_j}{2}\right\}.
$$

Using the change of variables, $\eta_j = \frac{1}{\omega_j}$, we obtain

$$
p(\eta_j \mid g, \gamma, \sigma^2, \lambda_g, \lambda_0, \theta_j) \propto \frac{1}{\eta_j^{3/2}} \exp\left\{\frac{-\eta_j(D_k g)_j^2 - \frac{\big((1-\theta_j)\lambda_0^2+\theta_j\lambda_g^2\big)v_{sc}(\gamma)}{\eta_j}}{2v_{sc}(\gamma)}\right\}.
$$

Thus, as in Step 5, we obtain,

$$
1/\omega_j \sim \textsc{Inverse-Gaussian}\left(\sqrt{\frac{\big((1-\theta_j)\lambda_0^2+\theta_j\lambda_g^2\big)v_{sc}(\gamma)}{|(D_k g)_j|^2}},\ (1-\theta_j)\lambda_0^2+\theta_j\lambda_g^2\right).
$$

Steps 6–7 of Appendix A.2.1

Drawing g : This follows directly from equations (5) and (6) as

$$
p(g \mid y, \sigma^2, \gamma, \omega) \propto p\big(y \mid g, \sigma^2, \gamma\big) \cdot p\big(g \mid \sigma^2, \gamma, \omega\big) \propto \exp\left\{-\frac{(y-g)'\mathcal{V}_\gamma^{-1}(y-g)}{2\sigma^2}\right\} \exp\left\{-\frac{g'\Sigma_g^{-1}g}{2v_{sc}(\gamma)}\right\}.
$$

Thus, as in Step 6, we obtain that

$$(g \mid y, \sigma^2, \gamma, \omega) \sim \mathcal{N}\left(\left(\mathcal{V}_\gamma^{-1} + \frac{\sigma^2}{v_{sc}(\gamma)}\Sigma_g^{-1}\right)^{-1} \mathcal{V}_\gamma^{-1} y,\ \sigma^2\left(\mathcal{V}_\gamma^{-1} + \frac{\sigma^2}{v_{sc}(\gamma)}\Sigma_g^{-1}\right)^{-1}\right).$$

Drawing λ_γ : We will make use of equations (12) and (13) along with

$$p(\gamma, \Sigma_\gamma) \propto \mathbb{1}_\gamma \cdot \det(\Sigma_\gamma)^{-\frac{1}{2}} \exp\left\{-\frac{1}{2}\gamma'\Sigma_\gamma^{-1}\gamma\right\} p(\Sigma_\gamma), \tag{A.8}$$

where $\mathbb{1}_\gamma = 1$ indicates a strictly stationary cycle. Assuming $\mathbb{1}_\gamma = 1$, integrating out Σ_γ simplifies the prior for γ to

$$p(\gamma \mid \lambda_\gamma) = \prod_{j=1}^{q}\left(\frac{\lambda_\gamma}{2}\exp\{-\lambda_\gamma|\gamma_j|\}\right),$$

so that

$$\begin{aligned} p(\lambda_\gamma \mid \gamma, r_\gamma, \delta_\gamma) &\propto p(\gamma \mid \lambda_\gamma, r_\gamma, \delta_\gamma) \cdot p(\lambda_\gamma \mid r, \delta) \\ &\propto \left(\prod_{j=1}^{q}\frac{\lambda_\gamma}{2}\exp\{-\lambda_\gamma|\gamma_j|\}\right) \cdot \lambda_\gamma^{r_\gamma - 1}\exp\{-\delta_\gamma\lambda_\gamma\}. \end{aligned}$$

Thus, as in Step 7, we obtain $(\lambda_\gamma \mid \gamma, r_\gamma, \delta_\gamma) \sim \Gamma\left(q + r_\gamma,\ \delta_\gamma + \sum_{j=1}^{q}|\gamma_j|\right)$.

Step 8 of Appendix A.2.1

Drawing $\Sigma_\gamma^{\mathrm{o}} \mid \gamma^{\mathrm{o}}$: This step consists of jointly drawing all τ_j and follows by similar steps as for ω_j. We have,

$$p(\tau_j \mid \gamma) \propto \det(\Sigma_\gamma)^{-\frac{1}{2}} \exp\left\{-\frac{1}{2}\gamma'\Sigma_\gamma^{-1}\gamma\right\} p(\Sigma_\gamma).$$

Using the change of variables, $\psi_j = \frac{1}{\tau_j}$, we obtain

$$p(\psi_j \mid \gamma) \propto \frac{1}{\psi_j^{3/2}} \exp\left\{-\frac{\psi_j \gamma_j^2 - (\lambda_\gamma)_j^2 \psi_j^{-1}}{2}\right\}.$$

Thus, we obtain $1/\tau_j^{\text{o}} \sim \text{INVERSE-GAUSSIAN}\left(\left|\frac{(\lambda_\gamma)_j}{\gamma_j}\right|,\ (\lambda_\gamma)_j^2\right)$.

Drawing $\gamma^{\text{o}} \mid \Sigma_\gamma^{\text{o}}$: Equations (A.5) and (A.6) imply that

$$\begin{aligned}
p(\gamma \mid c, g, \Sigma_g^{-1}, \Sigma_\gamma^{-1}, \sigma^2) &\propto p\big(c \mid \gamma, g, \sigma^2\big) \cdot p\big(\gamma \mid g, \Sigma_g^{-1}, \Sigma_\gamma^{-1}, \sigma^2\big) \\
&\propto p\big(c_{q+1:T} \mid c_{1:q}, \gamma, \sigma^2\big) \cdot p\big(c_{1:q} \mid \gamma, \sigma^2\big) \cdot p\big(g \mid \gamma, \Sigma_g^{-1}, \sigma^2\big) \cdot p\big(\gamma \mid \Sigma_\gamma^{-1}\big) \\
&\propto \exp\left\{-\frac{(CB'_{c,q} c_{q+1:T} - \gamma)' C^{-1} (CB'_{c,q} c_{q+1:T} - \gamma)}{2\sigma^2}\right\} \\
&\quad \times \frac{1}{(\mathcal{V}_{\gamma,11})^{(T-k)/2} |\mathcal{V}_\gamma|^{1/2}} \exp\left\{-\frac{c'_{1:q} \mathcal{V}_\gamma^{-1} c_{1:q}}{2\sigma^2}\right\} \exp\left\{-\frac{g' \Sigma_g^{-1} g}{2 v_{sc}(\gamma)}\right\}.
\end{aligned}$$

We cannot directly sample from this equation. However, following Del Negro, Giannone, Giannoni, and Tambalotti (2019), we use a Metropolis-Hastings step utilizing $\mathcal{N}\left(CB'_{c,q} c_{q+1:T},\ \sigma^2 C\right)$ as the candidate distribution. Let $\tilde{p}(\gamma, c, g, \Sigma_g^{-1}, \Sigma_\gamma^{-1}, \sigma^2)$ be its corresponding density. Starting at $\gamma^{(t)}$, we draw a candidate γ^{o} from the candidate distribution and calculate the acceptance probability α equal to

$$\begin{aligned}
&\min\left\{\frac{p\left(\gamma^{\text{o}} | c^{(t+1)}, \ldots, (\sigma^2)^{(t+1)}\right)}{p\left(\gamma^{(t)} | c^{(t+1)}, \ldots, (\sigma^2)^{(t+1)}\right)} \frac{\tilde{p}\left(\gamma^{(t)}, c^{(t+1)}, \ldots, (\sigma^2)^{(t+1)}\right)}{\tilde{p}\left(\gamma^{\text{o}}, c^{(t+1)}, \ldots, (\sigma^2)^{(t+1)}\right)},\ 1\right\} \\
&= \min\left\{\sqrt{\frac{v_{sc}(\gamma^{(t)})^{T-k} |\mathcal{V}_{\gamma^{(t)}}|}{v_{sc}(\gamma^{\text{o}})^{T-k} |\mathcal{V}_{\gamma^{\text{o}}}|}} \exp\left\{\frac{c'_{1:q}\left(\mathcal{V}_{\gamma^{(t)}}^{-1} - \mathcal{V}_{\gamma^{\text{o}}}^{-1}\right) c_{1:q}}{2\sigma^2} + \frac{g' \Sigma_g^{-1} g}{2\sigma^2}\left(\frac{1}{(v_{sc}(\gamma^{(t)})} - \frac{1}{v_{sc}(\gamma^{\text{o}})}\right)\right\},\ 1\right\}.
\end{aligned}$$

Our second accept-reject step is to take our candidate draw of $(\gamma^{\text{o}}, \Sigma_\gamma^{\text{o}})$ (drawn using the above procedure) and accept with probability $\alpha = \mathbb{1}_{\gamma^{\text{o}}}$, where $\mathbb{1}_{\gamma^{\text{o}}}$ is an indicator for whether γ^{o} produces a stationary cycle.

Table 1: **Level Model.** This table reports relative root mean-square error (RMSE) between the estimated and true trend for the level model. The benchmark model (with RMSE normalized to one) is the procedure introduced in Section 3 with $q = 4$ and $k = 2$. Values above 1 represent a larger RMSE as compared to the benchmark model. Each column reports a summary statistic of the RMSE across simulations: minimum, maximum, mean and the 5th, 10th, 50th, 90th, and 95th percentiles. The results are based on a sample size of $T = 250$ and $1,000$ simulations.

	Min.	5%	10%	50%	Mean	90%	95%	Max.
k=2 (no cycle)	1.56	1.50	1.46	1.38	1.36	1.28	1.27	1.24
HP Boost. (100)	1.41	1.38	1.36	1.29	1.28	1.22	1.21	1.20
HP Boost. (1600)	1.32	1.30	1.27	1.23	1.21	1.16	1.16	1.15
HP Boost. (14400)	1.18	1.21	1.21	1.16	1.16	1.11	1.11	1.13
Bior. Wavelet	1.24	1.21	1.19	1.15	1.15	1.12	1.12	1.13
Haar Wavelet	1.22	1.53	1.60	2.03	2.15	2.60	2.92	3.87
SSM Filter	1.05	1.08	1.06	1.08	1.12	1.18	1.29	1.78
SSM Smoother	0.93	0.93	0.93	0.98	1.07	1.23	1.38	2.67

Table 2: **Smooth Trend Model (Gaussian Cycle Innovations).** This table reports relative root mean-square error (RMSE) between the estimated and true trend for the smooth trend model with Gaussian cycle innovations. The benchmark model (with RMSE normalized to one) is the procedure introduced in Section 3 with $q = 4$ and $k = 2$. Values above 1 represent a larger RMSE as compared to the benchmark model. Each column reports a summary statistic of the RMSE across simulations: minimum, maximum, mean and the 5th, 10th, 50th, 90th, and 95th percentiles. The top panel reports results with homoskedastic cycle innovations. The bottom panel allows for stochastic volatility in the cycle innovations. The results are based on a sample size of $T = 250$ and $1,000$ simulations.

Homoskedasticity

	Min.	5%	10%	50%	Mean	90%	95%	Max.
k=1 (no cycle)	1.14	1.32	1.36	1.56	1.58	1.76	1.77	1.67
k=1 (with cycle)	0.98	0.96	0.96	0.96	0.96	0.96	0.96	0.96
k=2 (no cycle)	1.08	1.09	1.08	1.10	1.11	1.12	1.16	1.30
HP Boost. (100)	2.83	2.66	2.55	2.24	2.19	1.96	1.87	1.57
HP Boost. (1600)	2.33	2.20	2.12	1.91	1.87	1.68	1.63	1.40
HP Boost. (14400)	1.81	1.87	1.81	1.67	1.64	1.52	1.46	1.27
Bior. Wavelet	1.77	1.78	1.74	1.65	1.62	1.52	1.47	1.29
Haar Wavelet	1.20	1.24	1.28	1.36	1.35	1.41	1.42	1.36

Stochastic Volatility

	Min.	5%	10%	50%	Mean	90%	95%	Max.
k=1 (no cycle)	1.01	1.30	1.36	1.66	1.69	1.92	1.93	1.86
k=1 (with cycle)	0.97	0.96	0.97	0.96	0.96	0.96	0.95	1.45
k=2 (no cycle)	1.02	1.08	1.09	1.11	1.12	1.15	1.15	1.45
HP Boost. (100)	2.26	2.48	2.43	2.27	2.23	2.10	2.02	2.03
HP Boost. (1600)	1.97	2.05	2.03	1.93	1.89	1.80	1.73	1.87
HP Boost. (14400)	1.49	1.74	1.74	1.70	1.66	1.59	1.53	1.69
Bior. Wavelet	1.55	1.68	1.69	1.66	1.64	1.59	1.52	1.84
Haar Wavelet	1.17	1.26	1.30	1.35	1.34	1.35	1.34	1.22

Table 3: **Small Structural Break Trend Model (Gaussian Cycle Innovations).** This table reports relative root mean-square error (RMSE) between the estimated and true trend for the small structural break trend model with Gaussian cycle innovations. The benchmark model (with RMSE normalized to one) is the procedure introduced in Section 3 with $q = 4$ and $k = 2$. Values above 1 represent a larger RMSE as compared to the benchmark model. Each column reports a summary statistic of the RMSE across simulations: minimum, maximum, mean and the 5th, 10th, 50th, 90th, and 95th percentiles. The top panel reports results with homoskedastic cycle innovations. The bottom panel allows for stochastic volatility in the cycle innovations. The results are based on a sample size of $T = 250$ and $1,000$ simulations.

Homoskedasticity

	Min.	5%	10%	50%	Mean	90%	95%	Max.
k=1 (no cycle)	1.30	1.25	1.27	1.51	1.57	1.79	1.83	2.02
k=1 (with cycle)	1.03	0.97	0.96	0.95	0.96	0.97	0.98	1.01
k=2 (no cycle)	1.08	1.07	1.06	1.08	1.10	1.11	1.16	1.39
HP Boost. (100)	2.78	2.62	2.51	2.20	2.18	1.97	1.93	1.95
HP Boost. (1600)	2.29	2.14	2.09	1.87	1.86	1.71	1.67	1.73
HP Boost. (14400)	1.97	1.79	1.79	1.65	1.63	1.52	1.50	1.54
Bior. Wavelet	1.83	1.78	1.74	1.62	1.61	1.52	1.51	1.59
Haar Wavelet	1.35	1.29	1.29	1.32	1.35	1.39	1.42	1.55

Stochastic Volatility

	Min.	5%	10%	50%	Mean	90%	95%	Max.
k=1 (no cycle)	1.21	1.25	1.29	1.63	1.68	1.96	1.98	2.26
k=1 (with cycle)	1.03	0.96	0.97	0.96	0.96	0.97	0.98	1.28
k=2 (no cycle)	1.12	1.07	1.06	1.10	1.12	1.15	1.20	1.51
HP Boost. (100)	3.02	2.45	2.45	2.24	2.21	2.10	2.03	1.92
HP Boost. (1600)	2.43	2.05	2.02	1.92	1.88	1.81	1.75	1.66
HP Boost. (14400)	1.88	1.72	1.73	1.68	1.65	1.62	1.57	1.49
Bior. Wavelet	1.97	1.69	1.70	1.63	1.63	1.58	1.56	1.57
Haar Wavelet	1.43	1.30	1.30	1.33	1.32	1.34	1.33	1.34

Table 4: **Large Structural Break Trend Model (Chi-Square Cycle Innovations).** This table reports relative root mean-square error (RMSE) between the estimated and true trend for the large structural break trend model with chi-square cycle innovations. The benchmark model (with RMSE normalized to one) is the procedure introduced in Section 3 with $q = 4$ and $k = 2$. Values above 1 represent a larger RMSE as compared to the benchmark model. Each column reports a summary statistic of the RMSE across simulations: minimum, maximum, mean and the 5th, 10th, 50th, 90th, and 95th percentiles. The top panel reports results with homoskedastic cycle innovations. The bottom panel allows for stochastic volatility in the cycle innovations. The results are based on a sample size of $T = 250$ and $1,000$ simulations.

Homoskedasticity

	Min.	5%	10%	50%	Mean	90%	95%	Max.
k=1 (no cycle)	0.95	1.35	1.34	1.54	1.58	1.74	1.78	1.69
k=1 (with cycle)	0.53	0.89	0.92	0.98	1.00	1.03	1.15	1.52
k=2 (no cycle)	1.18	1.10	1.07	1.04	1.03	1.00	1.00	0.95
HP Boost. (100)	2.91	2.26	2.07	1.75	1.71	1.47	1.47	1.25
HP Boost. (1600)	2.40	1.90	1.74	1.50	1.46	1.28	1.26	1.10
HP Boost. (14400)	2.02	1.66	1.52	1.34	1.30	1.15	1.14	1.01
Bior. Wavelet	2.01	1.63	1.52	1.35	1.32	1.19	1.18	1.03
Haar Wavelet	1.10	1.17	1.26	1.56	1.63	1.85	1.99	2.34

Stochastic Volatility

	Min.	5%	10%	50%	Mean	90%	95%	Max.
k=1 (no cycle)	1.02	1.35	1.41	1.69	1.75	2.01	2.06	2.08
k=1 (with cycle)	0.69	0.90	0.92	1.02	1.10	1.26	1.54	2.07
k=2 (no cycle)	1.17	1.07	1.06	1.04	1.04	1.03	1.07	1.17
HP Boost. (100)	2.92	2.09	2.00	1.76	1.75	1.62	1.63	1.49
HP Boost. (1600)	2.55	1.77	1.71	1.51	1.50	1.39	1.38	1.35
HP Boost. (14400)	2.08	1.53	1.49	1.35	1.33	1.24	1.23	1.27
Bior. Wavelet	2.13	1.53	1.48	1.36	1.34	1.26	1.26	1.23
Haar Wavelet	1.15	1.15	1.25	1.54	1.61	1.84	1.94	2.14

Figure 1: **Time Series Properties of the Cross-Sectional Distribution of Forecasts.** This figure shows the cross-sectional median (solid line) and first and third quartiles (dashed lines) for the longer-run forecasts from the Survey of Primary Dealers (SPD). The real federal funds rate longer-run forecast is constructed by subtracting the individual longer-run PCE inflation forecast from the corresponding longer-run federal funds rate forecast. The sample period is July 2012 to March 2022.

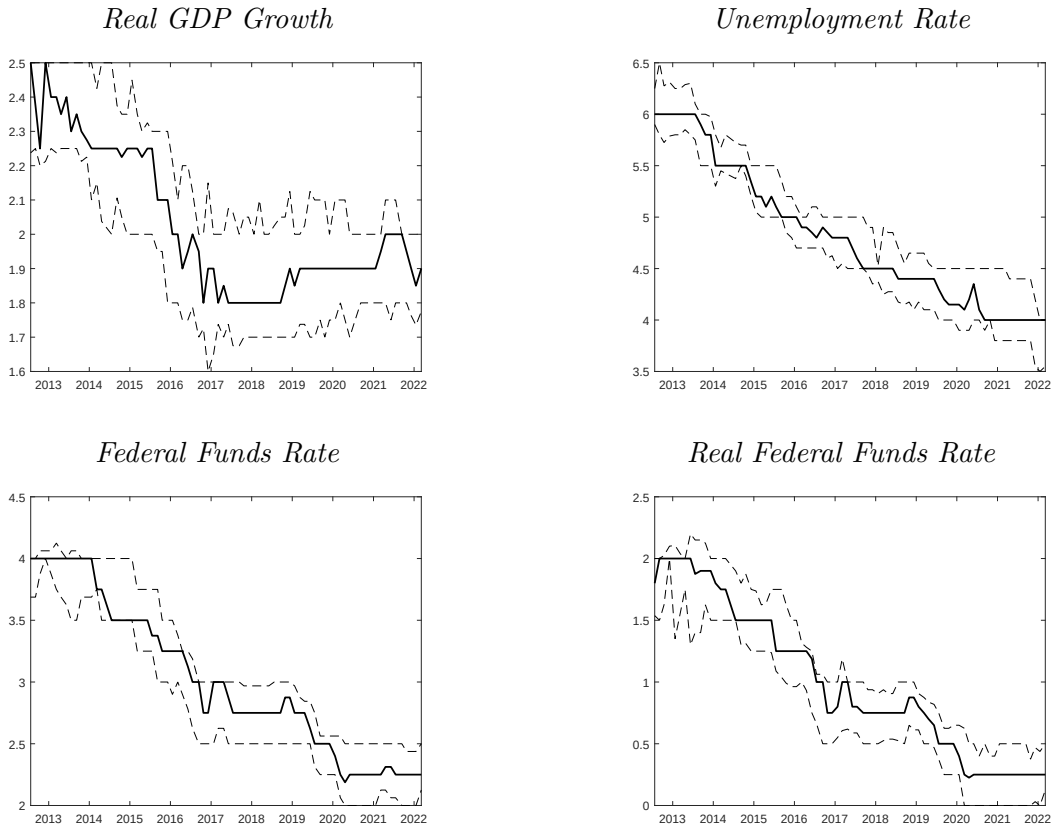

Figure 2: **Changes in Longer-Run Survey Forecasts.** This figure summarizes some of the properties of the changes in longer-run forecasts for real GDP growth, the unemployment rate, the federal funds rate and the real federal funds rate from the Survey of Primary Dealers. The top (bottom) panel displays the histogram of one-period changes (second differences) in longer-run forecasts. A medium grey hue denotes overlap in the pooled histogram and the optimally weighted histogram. The sample period is July 2012 to March 2022.

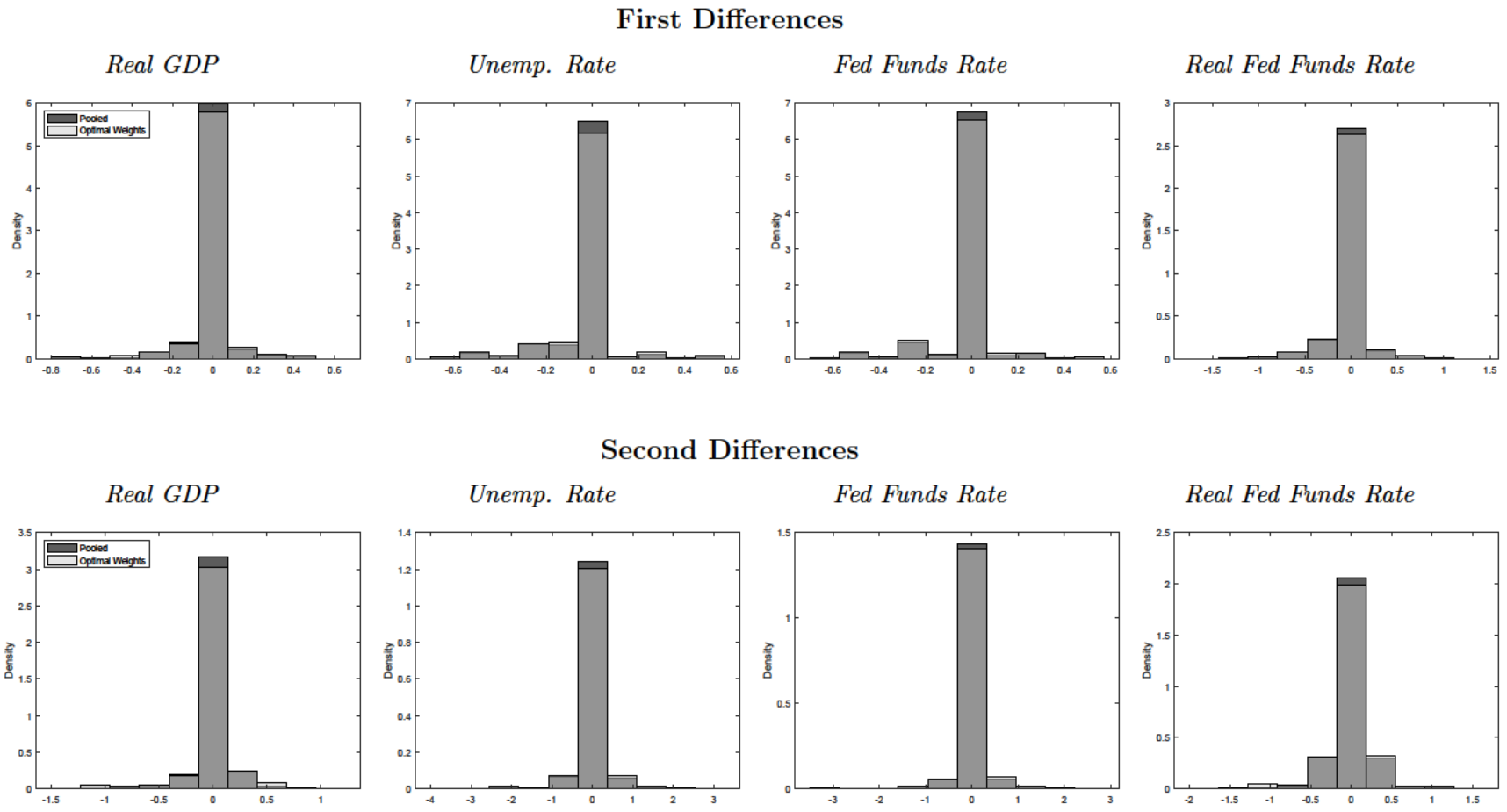

Figure 3: **Trend Estimates of the Annual Mean Temperature Change (°C) in the United States.** This figure presents trend estimates of the annual mean temperature change in the United States (expressed as a deviation from the average temperature over 1951–1980). The charts in the top row display the annual mean temperature change along with the estimated trend for $k = 1$ and $k = 2$ based on the methodology introduced in Section 3. Each chart displays the estimated trend with and without a (possibly) serially correlated cycle. The bottom row displays the estimated trend (posterior median) for $k = 2$ along with the corresponding 90% pointwise posterior coverage interval (left chart) and 90% uniform posterior coverage interval (right chart). The sample period is 1880–2023.

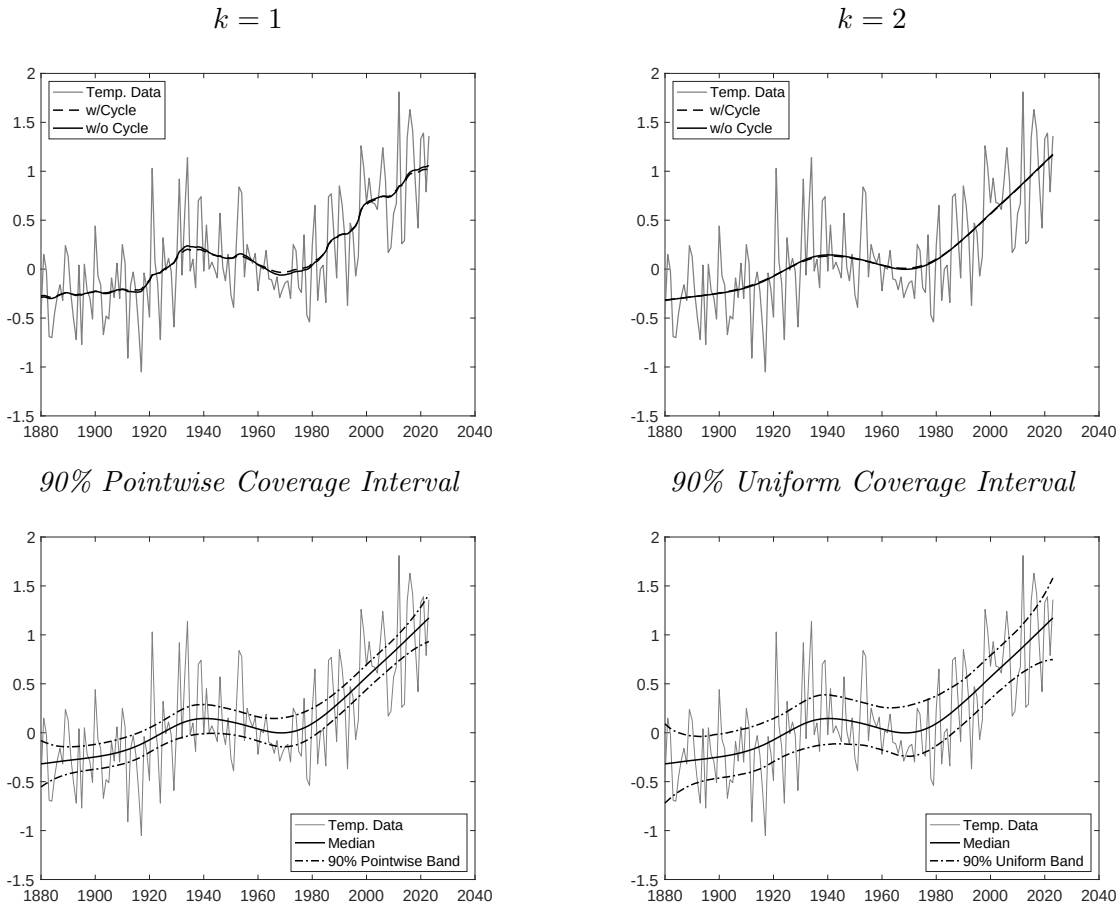

Figure 4: **Trend Estimate of Real GDP and Corresponding Output Gap.** This figure presents estimated trend and corresponding output gap based on the log level of real GDP. The left chart shows the time series of the log level of real GDP along with the estimated trend. The right chart shows the implied output gap based on the posterior median of the trend estimate. The sample period is 1947Q1–2023Q4. Grey shading denotes NBER recessions.

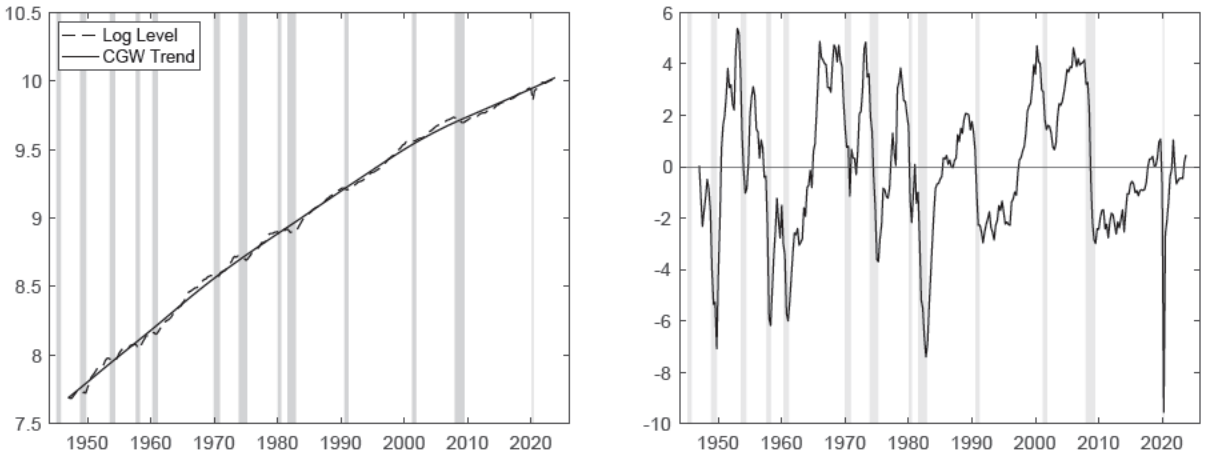

Figure 5: **Trend Estimates of Real GDP Growth.** This figure presents trend estimates of real GDP growth. The top left chart shows the implied trend growth estimate based on the log level of real GDP (black line) along with the 90% posterior coverage interval (dashed line). The top right chart present trend growth estimate based directly on real GDP growth (black line) along with the 90% posterior coverage interval (dashed line). In both charts, realized real GDP growth is denoted by the grey line. The bottom left chart shows the implied trend growth estimate based on the log level of real GDP along with the Bayesian unobserved components (BUC) model of Grant and Chan (2017b) and the Haar wavelet. The bottom right chart shows the implied trend growth estimate based on the log level of real GDP along with the HP filter (smoothing parameter 1,600), the HP boosting estimator of Phillips and Shi (2020), and the biorthogonal wavelet filter. The sample period is 1947Q2–2023Q4. Grey shading denotes NBER recessions.

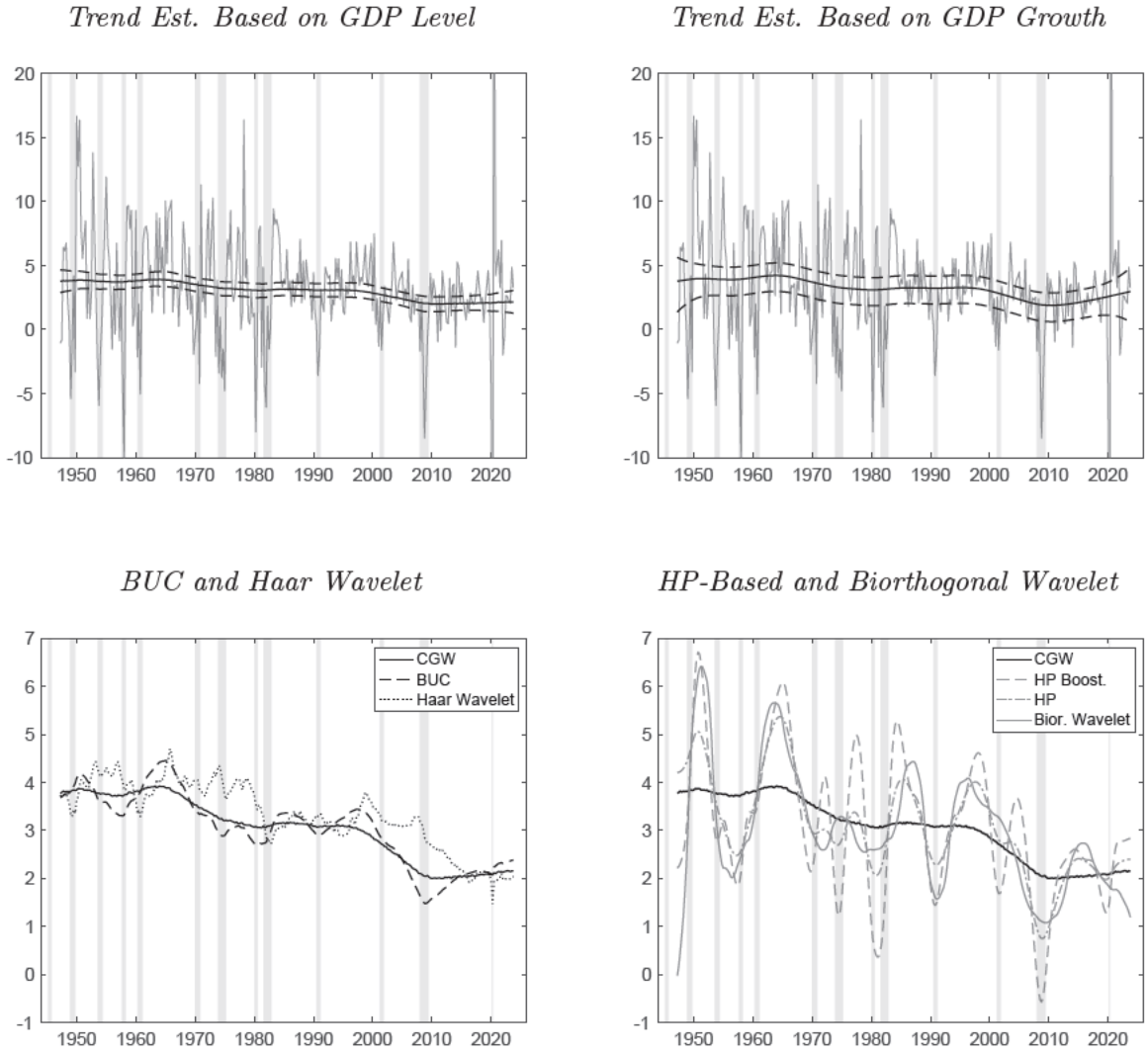

Figure 6: **Trend Estimates of Component Contributions to Real GDP Growth.** This figure presents trend estimates of component contributions to real GDP growth: personal consumption expenditures (PCE), residential investment, business fixed investment, federal government expenditures, state and local government expenditures, net exports and the change in inventories. All charts display the estimated trend (black line) and realized contributions (grey line). The bottom right chart compares the top-down estimate with the bottom-up estimate based on the sum of the individual components' trends. The sample period is 1947Q2–2023Q4. Grey shading denotes NBER recessions.

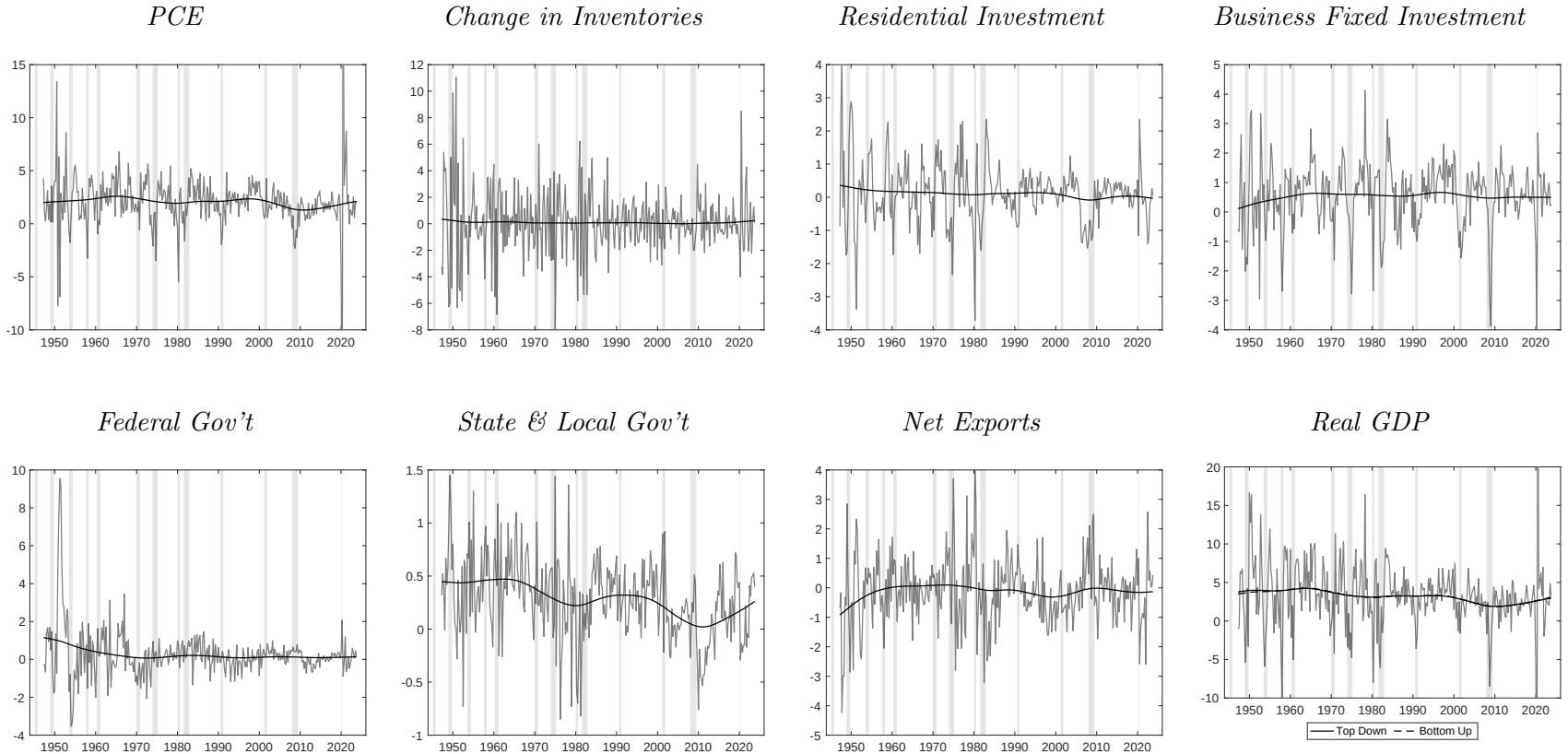

Supplemental Appendix:
"Sparse Trend Estimation"

Richard K. Crump (New York Fed)
Nikolay Gospodinov (Atlanta Fed)
Hunter Wieman (Princeton University)

SA.1 Gibbs Sampler: Trend Plus Noise

Throughout, we use the same notation as introduced in Section 3. In addition, define $S := \sum_{j=1}^{T-k} \theta_j$.

The steps of the Gibbs sampler are as follows:

1. Draw $(\lambda_g \mid g, \theta) \sim \Gamma\left(S + r_g,\ \delta_g + \sum \frac{\theta_j |(D_k g)_j|}{\sqrt{\sigma^2}}\right)$.

2. Draw $(\sigma^2 \mid y, g, \gamma) \sim \text{Inverse-Gamma}\left(T - \frac{k}{2},\ \frac{1}{2}\left((y-g)'(y-g) + g'\Sigma_g^{-1} g\right)\right)$.

3. Draw $(g \mid y, \sigma^2, \gamma, \omega) \sim \mathcal{N}\left(\left(I_T + \Sigma_g^{-1}\right)^{-1} y,\ \sigma^2 \left(I_T^{-1} + \Sigma_g^{-1}\right)^{-1}\right)$.

4. Draw $(\xi \mid \theta) \sim \mathcal{B}eta(S + a, T - k - S + b)$.

5. Draw each $(\theta_j \mid g, \sigma^2, \lambda_g, \lambda_0, \xi)$ as an independent Bernoulli random variable with

$$P(\theta_j = 0) = \frac{(1-\xi)\lambda_0 e^{-\sqrt{\lambda_0^2 (D_k g)_j^2 / \sigma^2}}}{(1-\xi)\lambda_0 e^{-\sqrt{\lambda_0^2 (D_k g)_j^2 / \sigma^2}} + \xi \lambda_g e^{-\sqrt{\lambda_g^2 (D_k g)_j^2 / \sigma^2}}},$$

$$P(\theta_j = 1) = \frac{\xi \lambda_g e^{-\sqrt{\lambda_g^2 (D_k g)_j^2 / \sigma^2}}}{(1-\xi)\lambda_0 e^{-\sqrt{\lambda_0^2 (D_k g)_j^2 / \sigma^2}} + \xi \lambda_g e^{-\sqrt{\lambda_g^2 (D_k g)_j^2 / \sigma^2}}},$$

   for $j = 1, \ldots, T-k$.

6. Draw each $(\frac{1}{\omega_j} \mid g, \theta_j, \lambda_g) \sim \text{Inverse-Gaussian}\left(\sqrt{\frac{\left((1-\theta_j)\lambda_0^2 + \theta_j \lambda_g^2\right)\sigma^2}{|(D_k g)_j|^2}},\ (1-\theta_j)\lambda_0^2 + \theta_j \lambda_g^2\right)$ independently for $j = 1, \ldots, T-k$.

We use the same choice of hyperparameters as in the case with a serially correlated cycle.

SA.2 Additional Simulations

In this section, we report additional simulation results to further assess the robustness of our procedure to non-Gaussian errors, the presence of stochastic volatility, and to different degrees of persistence in the cycle component. Tables SA.1–SA.9 show that, across all of these simulation designs, the new procedure we introduce in Section 3 outperforms the comparable alternatives.

Table SA.1: **Smooth Trend Model (Chi-Square Cycle Innovations).** This table reports relative root mean-square error (RMSE) between the estimated and true trend for the smooth trend model with chi-square cycle innovations. The benchmark model (with RMSE normalized to one) is the procedure introduced in Section 3 with $q = 4$ and $k = 2$. Values above 1 represent a larger RMSE as compared to the benchmark model. Each column reports a summary statistic of the RMSE across simulations: minimum, maximum, mean and the 5th, 10th, 50th, 90th, and 95th percentiles. The top panel reports results with homoskedastic cycle innovations. The bottom panel allows for stochastic volatility in the cycle innovations. The results are based on a sample size of $T = 250$ and $1,000$ simulations.

Homoskedasticity

	Min.	5%	10%	50%	Mean	90%	95%	Max.
k=1 (no cycle)	1.26	1.29	1.35	1.79	1.87	2.28	2.34	2.17
k=1 (with cycle)	0.92	0.98	0.96	0.97	1.03	1.04	1.27	1.88
k=2 (no cycle)	1.09	1.07	1.08	1.11	1.12	1.15	1.18	1.40
HP Boost. (100)	2.89	2.53	2.46	2.19	2.17	1.98	1.92	1.79
HP Boost. (1600)	2.14	2.14	2.06	1.87	1.85	1.73	1.67	1.60
HP Boost. (14400)	1.69	1.85	1.79	1.66	1.63	1.53	1.50	1.45
Bior. Wavelet	1.71	1.75	1.70	1.62	1.61	1.54	1.51	1.45
Haar Wavelet	1.20	1.27	1.26	1.33	1.34	1.37	1.39	1.32

Stochastic Volatility

	Min.	5%	10%	50%	Mean	90%	95%	Max.
k=1 (no cycle)	1.38	1.29	1.34	2.04	2.07	2.48	2.52	2.45
k=1 (with cycle)	0.93	0.95	0.97	0.98	1.17	1.51	1.90	2.37
k=2 (no cycle)	1.10	1.07	1.06	1.10	1.12	1.14	1.17	1.74
HP Boost. (100)	3.02	2.36	2.32	2.24	2.19	2.04	1.99	1.99
HP Boost. (1600)	2.12	1.97	1.96	1.90	1.87	1.76	1.73	1.78
HP Boost. (14400)	1.74	1.72	1.71	1.69	1.65	1.57	1.54	1.65
Bior. Wavelet	1.60	1.67	1.64	1.65	1.63	1.56	1.56	1.65
Haar Wavelet	1.37	1.24	1.26	1.33	1.32	1.32	1.30	1.25

Table SA.2: **Small Structural Break Trend Model (Chi-Square Cycle Innovations).** This table reports relative root mean-square error (RMSE) between the estimated and true trend for the small structural break trend model with chi-square cycle innovations. The benchmark model (with RMSE normalized to one) is the procedure introduced in Section 3 with $q = 4$ and $k = 2$. Values above 1 represent a larger RMSE as compared to the benchmark model. Each column reports a summary statistic of the RMSE across simulations: minimum, maximum, mean and the 5th, 10th, 50th, 90th, and 95th percentiles. The top panel reports results with homoskedastic cycle innovations. The bottom panel allows for stochastic volatility in the cycle innovations. The results are based on a sample size of $T = 250$ and $1,000$ simulations.

Homoskedasticity

	Min.	5%	10%	50%	Mean	90%	95%	Max.
k=1 (no cycle)	1.33	1.29	1.34	1.69	1.83	2.29	2.30	2.09
k=1 (with cycle)	1.04	0.98	0.97	0.96	1.02	1.04	1.12	1.86
k=2 (no cycle)	0.99	1.07	1.07	1.09	1.10	1.11	1.12	1.14
HP Boost. (100)	2.75	2.49	2.41	2.17	2.15	1.95	1.95	1.56
HP Boost. (1600)	2.30	2.06	2.02	1.85	1.83	1.69	1.64	1.38
HP Boost. (14400)	1.88	1.78	1.74	1.64	1.61	1.51	1.48	1.27
Bior. Wavelet	1.84	1.73	1.70	1.62	1.60	1.51	1.49	1.25
Haar Wavelet	1.18	1.22	1.24	1.31	1.32	1.40	1.41	1.47

Stochastic Volatility

	Min.	5%	10%	50%	Mean	90%	95%	Max.
k=1 (no cycle)	1.31	1.31	1.39	1.90	2.04	2.51	2.62	2.09
k=1 (with cycle)	1.09	1.00	0.98	0.98	1.12	1.28	1.80	2.03
k=2 (no cycle)	0.99	1.09	1.07	1.10	1.11	1.13	1.16	1.12
HP Boost. (100)	2.89	2.37	2.35	2.20	2.18	2.09	2.12	1.47
HP Boost. (1600)	2.25	1.99	1.97	1.88	1.86	1.78	1.78	1.34
HP Boost. (14400)	1.98	1.70	1.71	1.64	1.64	1.58	1.60	1.22
Bior. Wavelet	1.94	1.65	1.66	1.64	1.62	1.58	1.59	1.22
Haar Wavelet	1.22	1.23	1.25	1.31	1.30	1.36	1.36	1.09

Table SA.3: **Small Structural Break Trend Model (White-Noise Cycle, Gaussian Cycle Innovations).** This table reports relative root mean-square error (RMSE) between the estimated and true trend for the small structural break trend model with a white-noise cycle and Gaussian cycle innovations. The benchmark model (with RMSE normalized to one) is the procedure introduced in Section 3 with $q = 4$ and $k = 2$. Values above 1 represent a larger RMSE as compared to the benchmark model. Each column reports a summary statistic of the RMSE across simulations: minimum, maximum, mean and the 5th, 10th, 50th, 90th, and 95th percentiles. The top panel reports results with homoskedastic cycle innovations. The bottom panel allows for stochastic volatility in the cycle innovations. The results are based on a sample size of $T = 250$ and $1,000$ simulations.

Homoskedasticity

	Min.	5%	10%	50%	Mean	90%	95%	Max.
k=1 (no cycle)	1.01	0.98	0.97	0.97	0.98	0.99	0.99	1.05
k=1 (with cycle)	1.01	0.97	0.98	0.98	0.98	0.99	0.99	0.97
k=2 (no cycle)	0.97	1.00	1.00	1.00	1.00	1.00	1.01	0.99
HP Boost. (100)	1.87	1.85	1.86	1.81	1.79	1.72	1.70	1.85
HP Boost. (1600)	1.69	1.60	1.62	1.57	1.56	1.51	1.48	1.59
HP Boost. (14400)	1.45	1.39	1.41	1.40	1.38	1.35	1.35	1.42
Bior. Wavelet	1.50	1.44	1.45	1.42	1.41	1.38	1.38	1.50
Haar Wavelet	1.34	1.39	1.40	1.51	1.54	1.65	1.72	2.03

Stochastic Volatility

	Min.	5%	10%	50%	Mean	90%	95%	Max.
k=1 (no cycle)	1.01	0.98	0.99	0.98	0.98	0.99	0.99	1.02
k=1 (with cycle)	1.01	0.98	0.99	0.98	0.98	0.99	0.98	1.06
k=2 (no cycle)	0.94	1.00	1.00	1.00	1.00	1.00	1.00	1.01
HP Boost. (100)	1.91	1.77	1.81	1.82	1.82	1.87	1.81	1.71
HP Boost. (1600)	1.61	1.55	1.56	1.60	1.58	1.63	1.58	1.51
HP Boost. (14400)	1.37	1.35	1.38	1.42	1.41	1.45	1.43	1.37
Bior. Wavelet	1.51	1.40	1.41	1.43	1.43	1.45	1.46	1.46
Haar Wavelet	1.31	1.40	1.42	1.52	1.51	1.60	1.62	1.69

Table SA.4: **Small Structural Break Trend Model (White-Noise Cycle, Chi-Square Innovations).** This table reports relative root mean-square error (RMSE) between the estimated and true trend for the small structural break trend model with a white-noise cycle and chi-square cycle innovations. The benchmark model (with RMSE normalized to one) is the procedure introduced in Section 3 with $q = 4$ and $k = 2$. Values above 1 represent a larger RMSE as compared to the benchmark model. Each column reports a summary statistic of the RMSE across simulations: minimum, maximum, mean and the 5th, 10th, 50th, 90th, and 95th percentiles. The top panel reports results with homoskedastic cycle innovations. The bottom panel allows for stochastic volatility in the cycle innovations. The results are based on a sample size of $T = 250$ and $1,000$ simulations.

Homoskedasticity

	Min.	5%	10%	50%	Mean	90%	95%	Max.
k=1 (no cycle)	1.06	0.98	0.97	0.98	1.00	1.00	1.02	1.94
k=1 (with cycle)	1.08	0.98	0.98	0.98	1.02	1.02	1.04	2.27
k=2 (no cycle)	1.04	1.00	1.00	1.00	1.00	1.00	0.99	1.00
HP Boost. (100)	1.87	1.79	1.82	1.79	1.77	1.72	1.73	1.50
HP Boost. (1600)	1.64	1.60	1.59	1.55	1.54	1.49	1.48	1.34
HP Boost. (14400)	1.39	1.40	1.39	1.39	1.37	1.35	1.35	1.25
Bior. Wavelet	1.54	1.44	1.44	1.41	1.41	1.39	1.38	1.28
Haar Wavelet	1.16	1.33	1.34	1.50	1.53	1.65	1.73	1.99

Stochastic Volatility

	Min.	5%	10%	50%	Mean	90%	95%	Max.
k=1 (no cycle)	1.02	0.99	0.97	0.98	1.08	1.07	1.56	2.61
k=1 (with cycle)	1.08	0.99	0.97	0.99	1.09	1.07	1.63	2.65
k=2 (no cycle)	1.00	1.00	1.00	1.01	1.00	1.00	1.00	0.98
HP Boost. (100)	1.84	1.71	1.76	1.81	1.80	1.83	1.83	1.44
HP Boost. (1600)	1.69	1.52	1.55	1.58	1.57	1.58	1.57	1.27
HP Boost. (14400)	1.46	1.32	1.34	1.40	1.40	1.42	1.43	1.18
Bior. Wavelet	1.60	1.38	1.39	1.45	1.43	1.45	1.47	1.21
Haar Wavelet	1.15	1.33	1.36	1.49	1.50	1.62	1.66	1.45

Table SA.5: **Smooth Trend Model (White-Noise Cycle, Gaussian Cycle Innovations).** This table reports relative root mean-square error (RMSE) between the estimated and true trend for the smooth trend model with a white-noise cycle and Gaussian cycle innovations. The benchmark model (with RMSE normalized to one) is the procedure introduced in Section 3 with $q = 4$ and $k = 2$. Values above 1 represent a larger RMSE as compared to the benchmark model. Each column reports a summary statistic of the RMSE across simulations: minimum, maximum, mean and the 5th, 10th, 50th, 90th, and 95th percentiles. The top panel reports results with homoskedastic cycle innovations. The bottom panel allows for stochastic volatility in the cycle innovations. The results are based on a sample size of $T = 250$ and $1,000$ simulations.

Homoskedasticity

	Min.	5%	10%	50%	Mean	90%	95%	Max.
k=1 (no cycle)	1.01	0.98	0.97	0.97	0.98	0.99	0.99	1.05
k=1 (with cycle)	1.01	0.97	0.98	0.98	0.98	0.99	0.99	0.97
k=2 (no cycle)	0.97	1.00	1.00	1.00	1.00	1.00	1.01	0.99
HP Boost. (100)	1.87	1.85	1.86	1.81	1.79	1.72	1.70	1.85
HP Boost. (1600)	1.69	1.60	1.62	1.57	1.56	1.51	1.48	1.59
HP Boost. (14400)	1.45	1.39	1.41	1.40	1.38	1.35	1.35	1.42
Bior. Wavelet	1.50	1.44	1.45	1.42	1.41	1.38	1.38	1.50
Haar Wavelet	1.34	1.39	1.40	1.51	1.54	1.65	1.72	2.03

Stochastic Volatility

	Min.	5%	10%	50%	Mean	90%	95%	Max.
k=1 (no cycle)	1.01	0.98	0.99	0.98	0.98	0.99	0.99	1.02
k=1 (with cycle)	1.01	0.98	0.99	0.98	0.98	0.99	0.98	1.06
k=2 (no cycle)	0.94	1.00	1.00	1.00	1.00	1.00	1.00	1.01
HP Boost. (100)	1.91	1.77	1.81	1.82	1.82	1.87	1.81	1.71
HP Boost. (1600)	1.61	1.55	1.56	1.60	1.58	1.63	1.58	1.51
HP Boost. (14400)	1.37	1.35	1.38	1.42	1.41	1.45	1.43	1.37
Bior. Wavelet	1.51	1.40	1.41	1.43	1.43	1.45	1.46	1.46
Haar Wavelet	1.31	1.40	1.42	1.52	1.51	1.60	1.62	1.69

Table SA.6: **Smooth Trend Model (White-Noise Cycle, Chi-Square Cycle Innovations).** This table reports relative root mean-square error (RMSE) between the estimated and true trend for the smooth trend model with a white-noise cycle and chi-square cycle innovations. The benchmark model (with RMSE normalized to one) is the procedure introduced in Section 3 with $q = 4$ and $k = 2$. Values above 1 represent a larger RMSE as compared to the benchmark model. Each column reports a summary statistic of the RMSE across simulations: minimum, maximum, mean and the 5th, 10th, 50th, 90th, and 95th percentiles. The top panel reports results with homoskedastic cycle innovations. The bottom panel allows for stochastic volatility in the cycle innovations. The results are based on a sample size of $T = 250$ and $1,000$ simulations.

Homoskedasticity

	Min.	5%	10%	50%	Mean	90%	95%	Max.
k=1 (no cycle)	1.06	0.98	0.97	0.98	1.00	1.00	1.02	1.94
k=1 (with cycle)	1.08	0.98	0.98	0.98	1.02	1.02	1.04	2.27
k=2 (no cycle)	1.04	1.00	1.00	1.00	1.00	1.00	0.99	1.00
HP Boost. (100)	1.87	1.79	1.82	1.79	1.77	1.72	1.73	1.50
HP Boost. (1600)	1.64	1.60	1.59	1.55	1.54	1.49	1.48	1.34
HP Boost. (14400)	1.39	1.40	1.39	1.39	1.37	1.35	1.35	1.25
Bior. Wavelet	1.54	1.44	1.44	1.41	1.41	1.39	1.38	1.28
Haar Wavelet	1.16	1.33	1.34	1.50	1.53	1.65	1.73	1.99

Stochastic Volatility

	Min.	5%	10%	50%	Mean	90%	95%	Max.
k=1 (no cycle)	1.02	0.99	0.97	0.98	1.08	1.07	1.56	2.61
k=1 (with cycle)	1.08	0.99	0.97	0.99	1.09	1.07	1.63	2.65
k=2 (no cycle)	1.00	1.00	1.00	1.01	1.00	1.00	1.00	0.98
HP Boost. (100)	1.84	1.71	1.76	1.81	1.80	1.83	1.83	1.44
HP Boost. (1600)	1.69	1.52	1.55	1.58	1.57	1.58	1.57	1.27
HP Boost. (14400)	1.46	1.32	1.34	1.40	1.40	1.42	1.43	1.18
Bior. Wavelet	1.60	1.38	1.39	1.45	1.43	1.45	1.47	1.21
Haar Wavelet	1.15	1.33	1.36	1.49	1.50	1.62	1.66	1.45

Table SA.7: **Large Structural Break Trend Model (Gaussian Cycle Innovations).** This table reports relative root mean-square error (RMSE) between the estimated and true trend for the large structural break trend model with Gaussian cycle innovations. The benchmark model (with RMSE normalized to one) is the procedure introduced in Section 3 with $q = 4$ and $k = 2$. Values above 1 represent a larger RMSE as compared to the benchmark model. Each column reports a summary statistic of the RMSE across simulations: minimum, maximum, mean and the 5th, 10th, 50th, 90th, and 95th percentiles. The top panel reports results with homoskedastic cycle innovations. The bottom panel allows for stochastic volatility in the cycle innovations. The results are based on a sample size of $T = 250$ and $1,000$ simulations.

Homoskedasticity

	Min.	5%	10%	50%	Mean	90%	95%	Max.
k=1 (no cycle)	1.05	1.25	1.28	1.37	1.37	1.42	1.43	1.31
k=1 (with cycle)	0.43	0.87	0.92	0.95	0.94	0.94	0.93	0.91
k=2 (no cycle)	1.15	1.07	1.05	1.03	1.03	1.01	1.00	0.95
HP Boost. (100)	3.68	2.32	2.10	1.74	1.73	1.49	1.45	1.28
HP Boost. (1600)	3.05	1.92	1.76	1.50	1.48	1.30	1.26	1.14
HP Boost. (14400)	2.59	1.63	1.52	1.33	1.31	1.17	1.15	1.02
Bior. Wavelet	2.60	1.65	1.53	1.33	1.33	1.20	1.18	1.05
Haar Wavelet	0.99	1.19	1.26	1.55	1.63	1.85	2.01	2.30

Stochastic Volatility

	Min.	5%	10%	50%	Mean	90%	95%	Max.
k=1 (no cycle)	0.87	1.28	1.28	1.42	1.47	1.57	1.56	1.75
k=1 (with cycle)	0.67	0.87	0.91	0.96	0.95	0.97	0.97	1.10
k=2 (no cycle)	1.23	1.08	1.06	1.03	1.04	1.03	1.05	1.21
HP Boost. (100)	4.38	2.17	2.01	1.75	1.76	1.64	1.59	1.50
HP Boost. (1600)	3.55	1.82	1.68	1.50	1.51	1.42	1.38	1.29
HP Boost. (14400)	2.74	1.58	1.46	1.33	1.34	1.26	1.23	1.18
Bior. Wavelet	2.87	1.58	1.50	1.33	1.35	1.27	1.24	1.23
Haar Wavelet	1.04	1.20	1.27	1.51	1.61	1.82	1.93	2.27

Table SA.8: **Large Structural Break Trend Model (White-Noise Cycle, Gaussian Cycle Innovations).** This table reports relative root mean-square error (RMSE) between the estimated and true trend for the large structural break trend model with a white-noise cycle and Gaussian cycle innovations. The benchmark model (with RMSE normalized to one) is the procedure introduced in Section 3 with $q = 4$ and $k = 2$. Values above 1 represent a larger RMSE as compared to the benchmark model. Each column reports a summary statistic of the RMSE across simulations: minimum, maximum, mean and the 5th, 10th, 50th, 90th, and 95th percentiles. The top panel reports results with homoskedastic cycle innovations. The bottom panel allows for stochastic volatility in the cycle innovations. The results are based on a sample size of $T = 250$ and $1,000$ simulations.

Homoskedasticity

	Min.	5%	10%	50%	Mean	90%	95%	Max.
k=1 (no cycle)	0.46	0.85	0.86	0.89	0.87	0.84	0.83	0.69
k=1 (with cycle)	0.48	0.87	0.86	0.90	0.88	0.85	0.83	0.72
k=2 (no cycle)	0.92	0.99	1.00	0.99	0.98	0.96	0.94	0.74
HP Boost. (100)	2.81	1.84	1.67	1.39	1.36	1.16	1.12	0.92
HP Boost. (1600)	2.58	1.59	1.47	1.24	1.21	1.03	1.01	0.84
HP Boost. (14400)	2.14	1.41	1.31	1.12	1.10	0.97	0.95	0.77
Bior. Wavelet	2.25	1.47	1.35	1.17	1.15	1.01	1.00	0.79
Haar Wavelet	0.90	1.20	1.36	1.80	1.88	2.14	2.31	2.45

Stochastic Volatility

	Min.	5%	10%	50%	Mean	90%	95%	Max.
k=1 (no cycle)	0.55	0.84	0.84	0.89	0.88	0.86	0.86	0.78
k=1 (with cycle)	0.61	0.85	0.86	0.90	0.88	0.86	0.88	0.87
k=2 (no cycle)	0.91	0.99	1.00	0.99	0.98	0.95	0.95	0.83
HP Boost. (100)	3.22	1.71	1.59	1.41	1.40	1.27	1.25	1.04
HP Boost. (1600)	2.86	1.52	1.38	1.24	1.23	1.12	1.11	0.90
HP Boost. (14400)	2.29	1.35	1.26	1.13	1.12	1.02	1.02	0.85
Bior. Wavelet	2.43	1.41	1.31	1.18	1.17	1.06	1.08	0.90
Haar Wavelet	0.88	1.26	1.35	1.77	1.85	2.09	2.27	2.37

Table SA.9: **Large Structural Break Trend Model (White-Noise Cycle, Chi-Square Cycle Innovations).** This table reports relative root mean-square error (RMSE) between the estimated and true trend for the large structural break trend model with a white-noise cycle and chi-square cycle innovations. The benchmark model (with RMSE normalized to one) is the procedure introduced in Section 3 with $q = 4$ and $k = 2$. Values above 1 represent a larger RMSE as compared to the benchmark model. Each column reports a summary statistic of the RMSE across simulations: minimum, maximum, mean and the 5th, 10th, 50th, 90th, and 95th percentiles. The top panel reports results with homoskedastic cycle innovations. The bottom panel allows for stochastic volatility in the cycle innovations. The results are based on a sample size of $T = 250$ and $1,000$ simulations.

Homoskedasticity

	Min.	5%	10%	50%	Mean	90%	95%	Max.
k=1 (no cycle)	0.43	0.85	0.89	0.90	0.91	0.90	0.95	1.41
k=1 (with cycle)	0.50	0.83	0.89	0.91	0.92	0.91	0.97	1.39
k=2 (no cycle)	0.98	1.00	1.01	1.00	0.98	0.97	0.96	0.88
HP Boost. (100)	2.21	1.79	1.67	1.39	1.35	1.18	1.14	0.94
HP Boost. (1600)	2.07	1.56	1.48	1.22	1.20	1.05	1.01	0.84
HP Boost. (14400)	1.77	1.40	1.30	1.13	1.10	0.98	0.95	0.84
Bior. Wavelet	1.98	1.45	1.36	1.18	1.15	1.03	1.01	0.91
Haar Wavelet	0.97	1.20	1.31	1.80	1.88	2.16	2.31	2.67

Stochastic Volatility

	Min.	5%	10%	50%	Mean	90%	95%	Max.
k=1 (no cycle)	0.64	0.85	0.90	0.93	0.99	1.05	1.30	2.20
k=1 (with cycle)	0.66	0.87	0.91	0.93	1.01	1.07	1.40	2.24
k=2 (no cycle)	0.99	1.01	1.00	0.99	0.98	0.97	0.97	1.00
HP Boost. (100)	2.39	1.69	1.63	1.40	1.39	1.27	1.25	1.21
HP Boost. (1600)	2.08	1.47	1.45	1.23	1.22	1.12	1.10	1.08
HP Boost. (14400)	1.91	1.33	1.29	1.13	1.12	1.03	1.01	1.01
Bior. Wavelet	1.99	1.38	1.34	1.18	1.17	1.09	1.08	1.00
Haar Wavelet	1.01	1.17	1.35	1.78	1.85	2.13	2.26	2.59

SA.3 Additional Results: Priors and Posteriors

In this section, we provide some additional results related to the empirical applications presented in the main text. Figure SA.1 presents the prior density for λ_g which follows a Gamma distribution with shape and rate parameters as described in Section A.2.1 of the main text. The charts also show a histogram of the 50,000 posterior draws of λ_g. In the top row we present the results for real GDP growth in levels (top left chart) and growth rates (top right chart). In the bottom row we present the results for annual mean temperature change for $k = 1$ (bottom left chart) and $k = 2$ (bottom right chart). Figure SA.1 reveals the diffuse nature of our prior choice for λ_g and that the posterior estimates have resulting distributions which are substantially more concentrated.

As we have emphasized in the main text, the SPD survey data have motivated the choice of prior density for innovations to the trend in our procedure. To clarify the link between the properties of the SPD data that we use to motivate the prior and the posterior draws from our procedure, in Figure SA.2 we plot three selected posterior draws for the climate application. The left chart of Figure SA.2 shows posterior draws for $k = 1$ and $q = 4$. We can observe discrete shifts in each draw which corresponds to a high probability mass near zero in its first difference. This is shown explicitly in the right chart in Figure SA.2 where very small changes and larger changes in the time series appear to be decoupled.

Furthermore, we consider a robustness exercise with different prior choices for λ_g. We vary the prior mean across three additional values (means of 30, 100 and 1000) along with our baseline implementation choice as given in the main text (mean of 300). In Figure SA.3, we present the trend estimates across this range of values for the prior mean on λ_g. The left chart presents the results when using the (log) level of real GDP and the right chart when using real GDP growth. For either target series, the trend estimates are very similar across the different prior specifications. Moreover, the trend estimates are much more tightly bunched with only small deviations as compared to, for example, the gap between the conventional HP filter and HP boosting (as shown in the main text).

Next, we show histograms of 50,000 posterior draws of λ_g. These histograms are shown in Figure SA.4 (for the level of real GDP) and Figure SA.5 (for real GDP growth). As the figures show, the distribution of the posterior draws of λ_g are very similar across prior specifications (as

illustrated by the bottom chart), and they can diverge noticeably from their prior distribution.

Finally, we also report the prior and posterior distribution for the model-implied signal-to-noise ratio: $\frac{2(1-\xi)}{\lambda_0^2} + \frac{2\xi}{\lambda_g^2}$. In Figures SA.6 and SA.7 we show the prior and posterior draws of the (log) signal-to-noise ratio for the four different choices of prior specifications for λ_g. These figures show that the posterior distribution of the signal-to-noise ratio is very similar across the whole range of prior specifications suggesting that this distribution is insensitive to the prior choice (as illustrated by the bottom chart). Furthermore, when the prior mean for λ_g is 30 or 100, there is considerable probability mass placed on high signal-to-noise ratios. Nonetheless, in all of these cases the CGW filter still produces posterior distributions concentrated at low signal-to-noise ratios and trend estimates that are substantially less variable than those produced by, for example, the conventional HP filter.

Figure SA.1: λ_g**: Prior Distribution and Posterior Draws.** This figure presents the prior density for λ_g (red line; see Section A.2.1 in the main text) along with 50,000 posterior draws for λ_g (blue bars) for the two empirical applications in the main text.

Real GDP (Level)

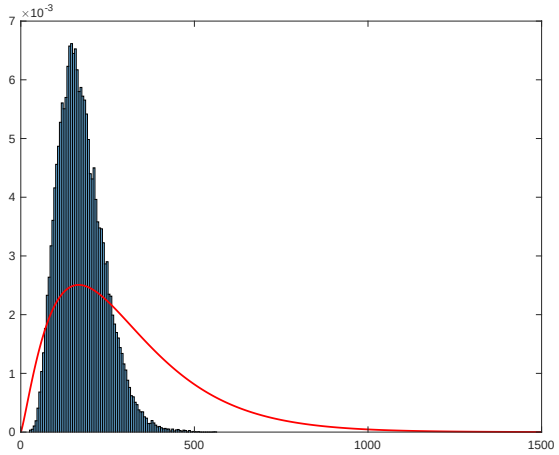

Real GDP (Growth Rate)

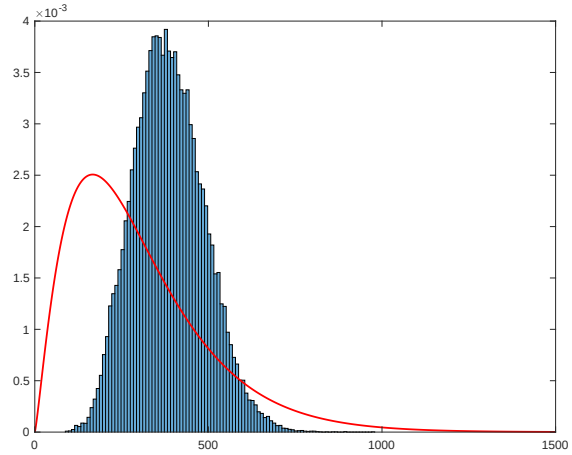

Annual Mean Temperature Change ($k = 1$)

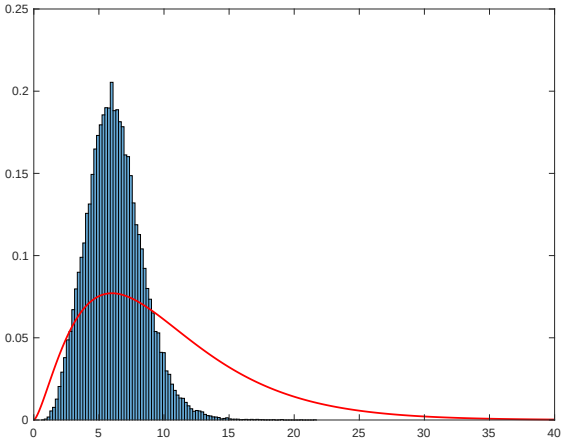

Annual Mean Temperature Change ($k = 2$)

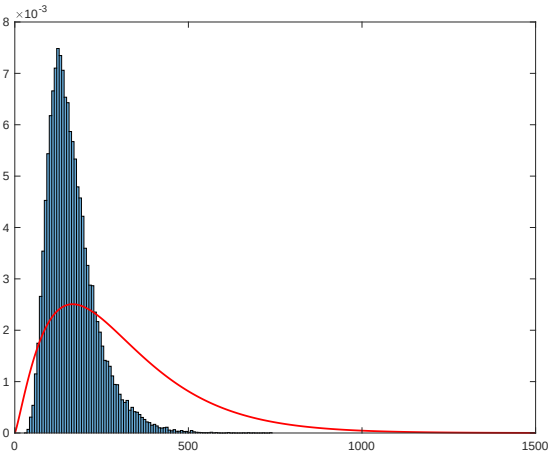

Figure SA.2: **Trend Estimates of the Annual Mean Temperature Change: Selected Posterior Draws.** This figure shows three posterior draws for the choice of $k = 1$. The left chart shows the time series of each posterior draw of the trend estimate. The right chart shows the corresponding histogram of the change in the posterior trend estimate.

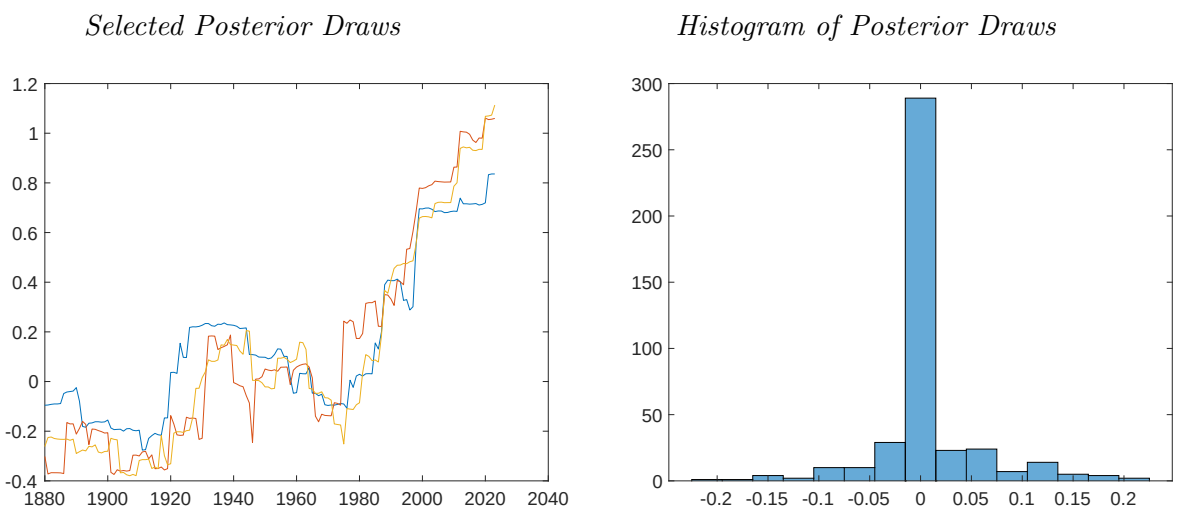

Figure SA.3: **Trend Estimates of Real GDP Growth Across a Range of Prior Specifications** This figure shows the trend estimate for real GDP growth using the CGW procedure for $k = 2$ and $q = 4$ across a range of different prior distributions corresponding to prior means of $\{30, 100, 300, 1000\}$. The left chart presents the trend estimates using the (log) level of real GDP and the right chart for real GDP growth. Both charts also present the trend estimate based on HP boosting (dashed line).

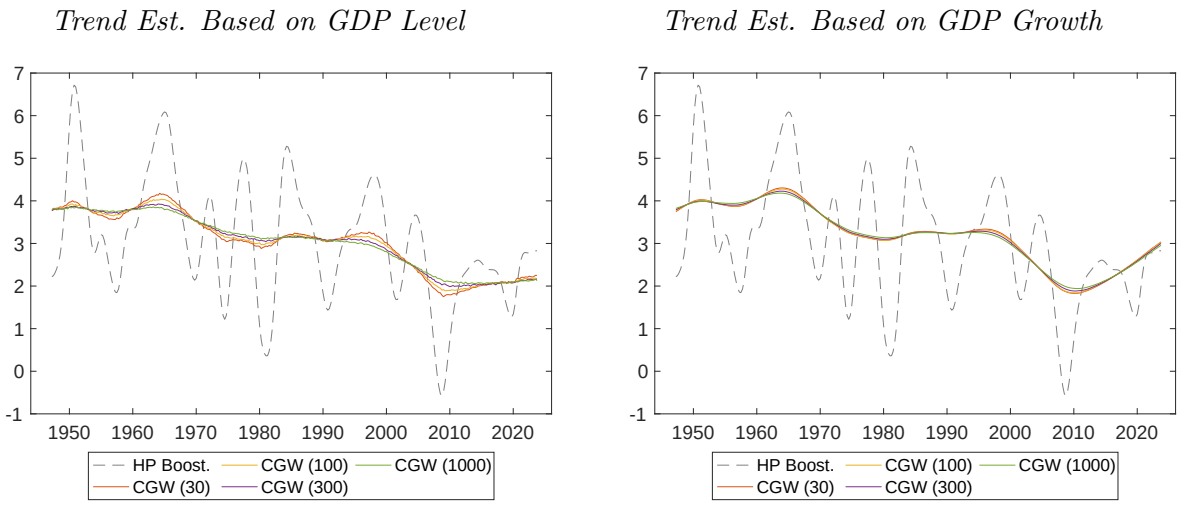

Figure SA.4: **Prior and Posterior Draws of λ_g for Trend Estimates using Level of Real GDP** This figure shows prior and posterior draws of λ_g for the CGW procedure for $k = 2$ and $q = 4$ applied to the (log) level of real GDP across a range of different prior distributions corresponding to prior means of $\{30, 100, 300, 1000\}$.

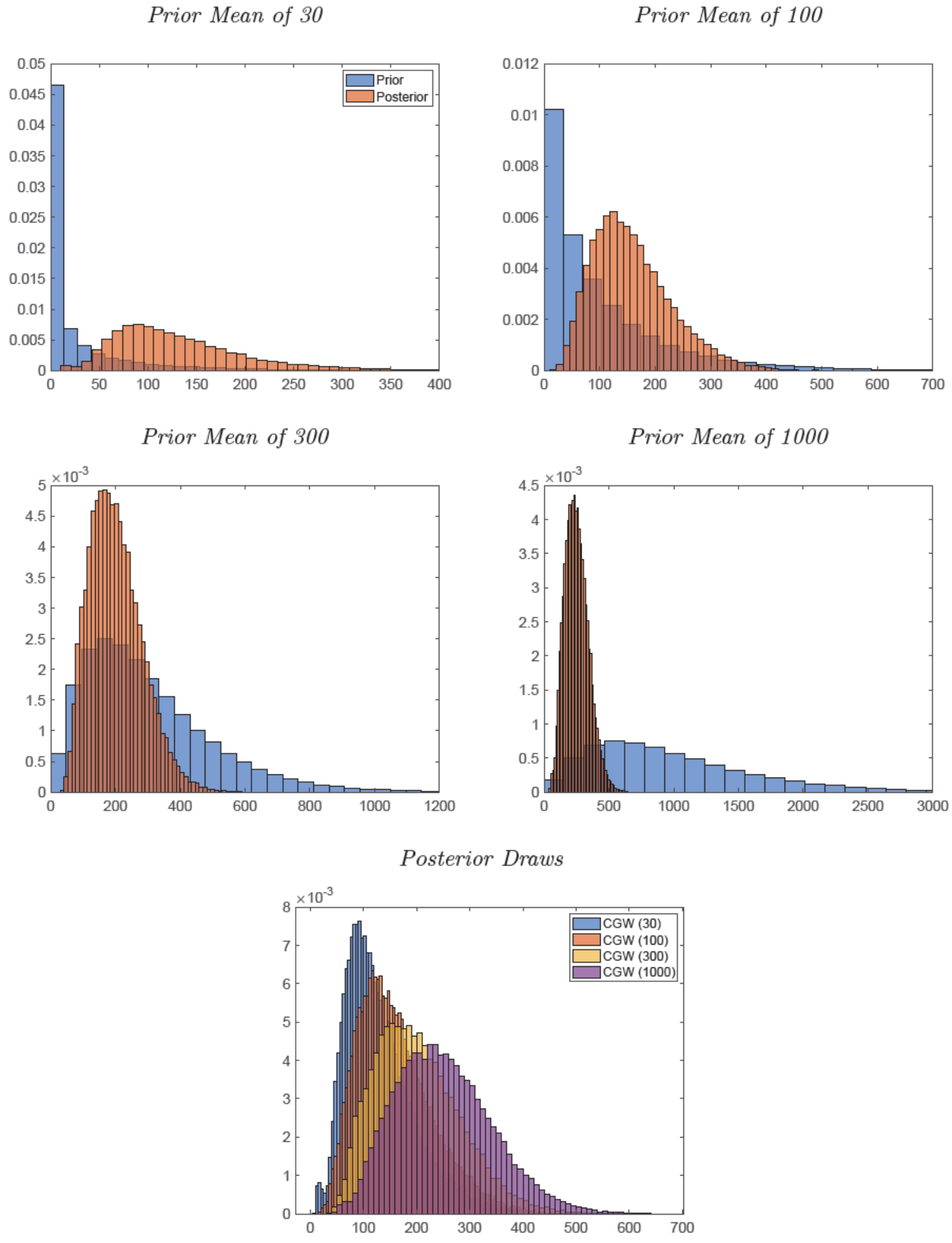

Figure SA.5: **Prior and Posterior Draws of λ_g for Trend Estimates using Real GDP Growth** This figure shows prior and posterior draws of λ_g for the CGW procedure for $k = 2$ and $q = 4$ applied to real GDP growth across a range of different prior distributions corresponding to prior means of $\{30, 100, 300, 1000\}$.

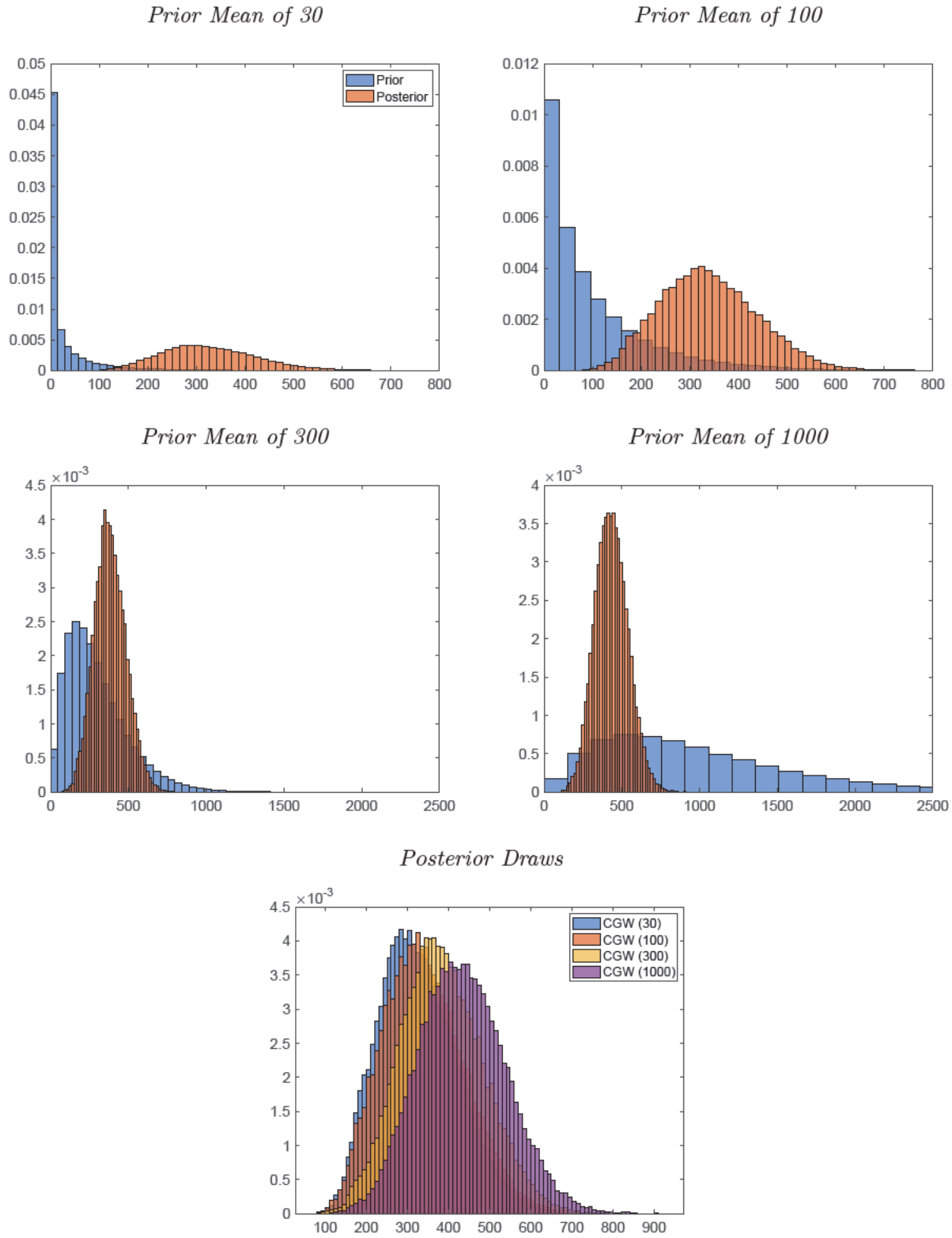

Figure SA.6: **Prior and Posterior Signal-to-Noise Draws for Trend Estimates using Level of Real GDP** This figure shows prior and posterior draws of the signal-to-noise ratio for the CGW procedure for $k = 2$ and $q = 4$ applied to the (log) level of real GDP across a range of different prior distributions corresponding to prior means of $\{30, 100, 300, 1000\}$. The red vertical line indicates the signal-to-noise ratio for the HP filter when using a smoothing parameter of 1,600.

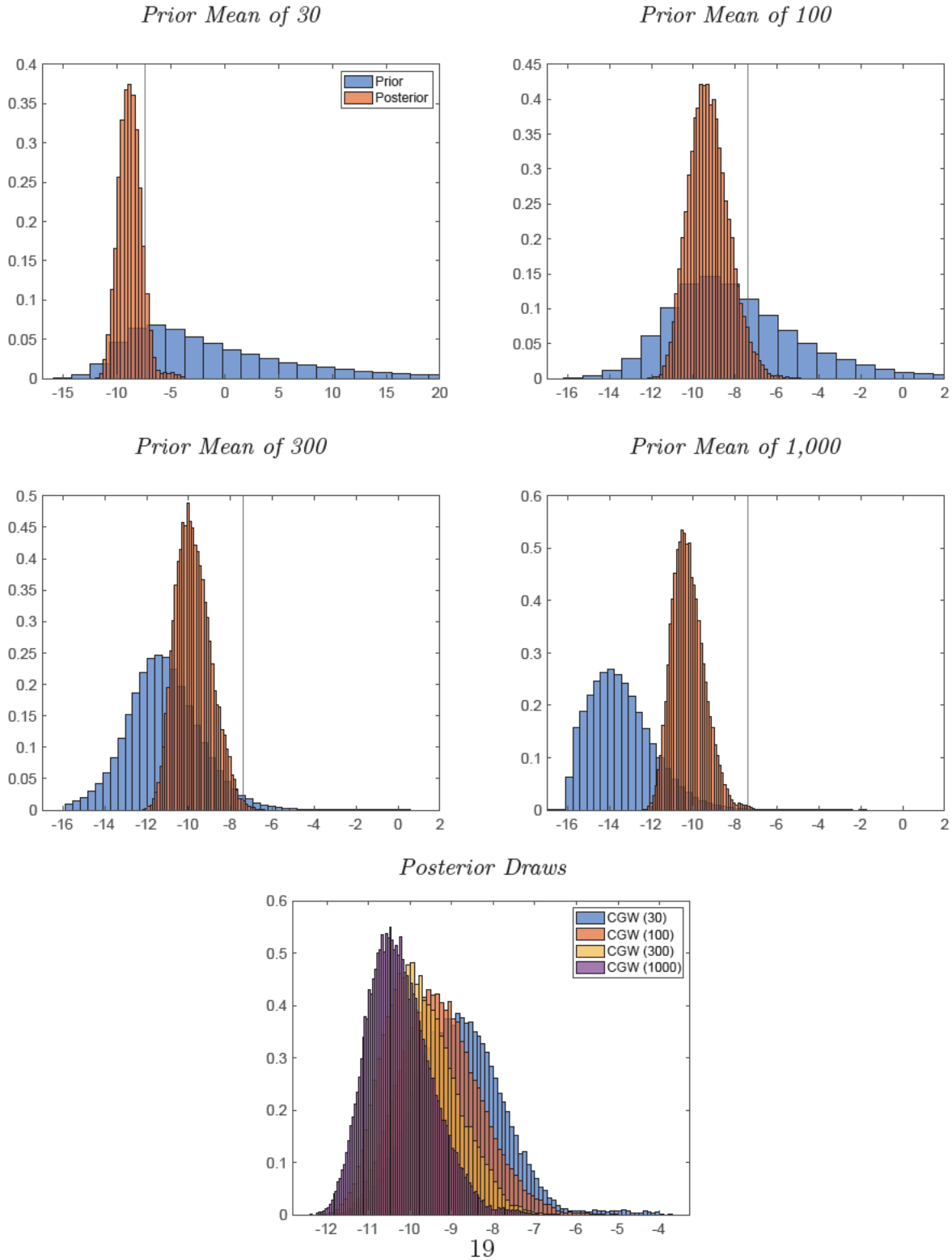

Figure SA.7: **Prior and Posterior Signal-to-Noise Draws for Trend Estimates using Real GDP Growth** This figure shows prior and posterior draws of the signal-to-noise ratio for the CGW procedure for $k = 2$ and $q = 4$ applied to real GDP growth across a range of different prior distributions corresponding to prior means of $\{30, 100, 300, 1000\}$. The red vertical line indicates the signal-to-noise ratio for the HP filter when using a smoothing parameter of 1,600.

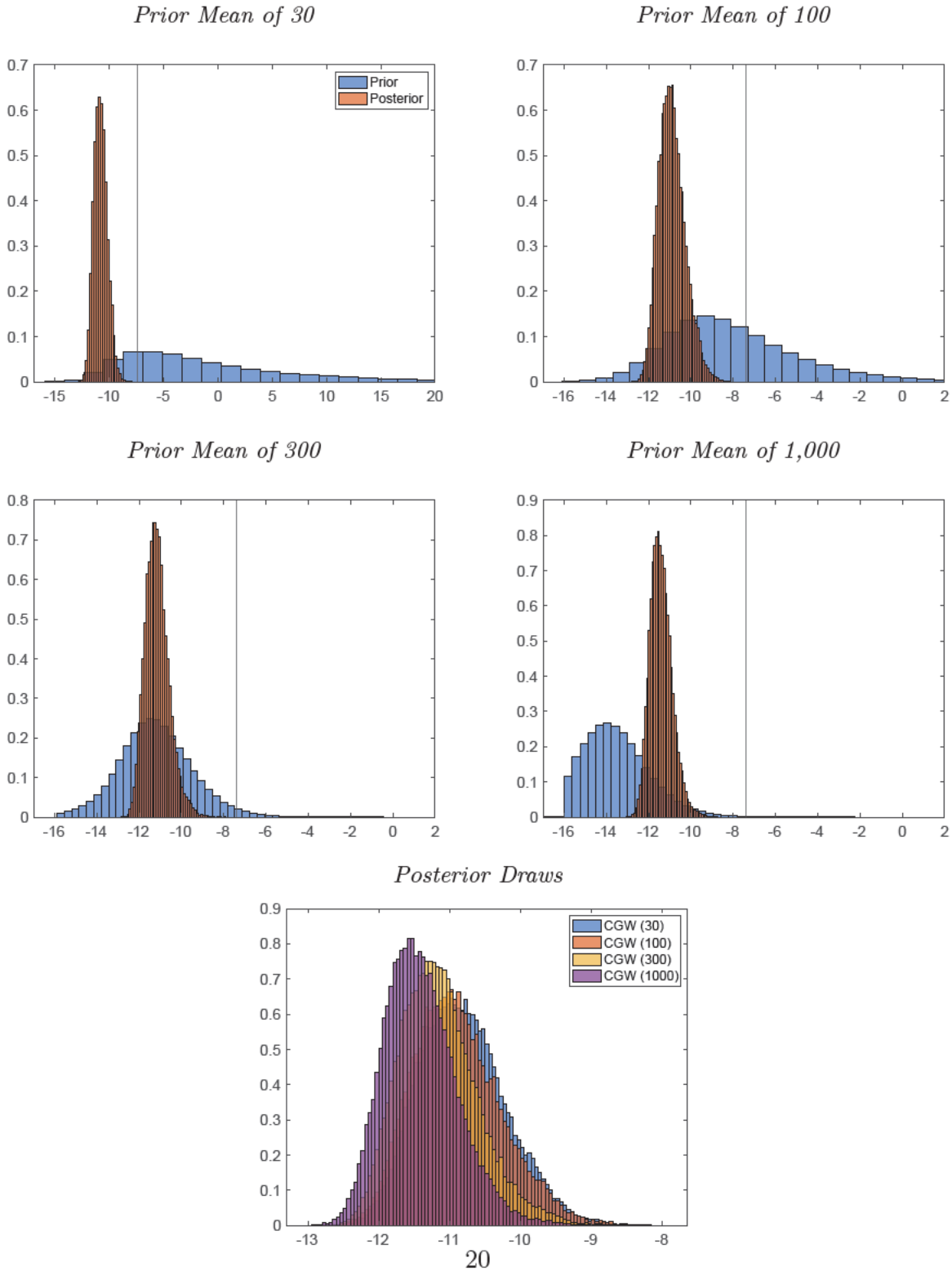

SA.4 Additional Empirical Application: Total Factor Productivity (TFP) Growth

As an additional empirical application, we investigate the underlying trend in U.S. total factor productivity (TFP) growth. Quarterly data for the period 1947:Q2–2023:Q4 are obtained from the Federal Reserve Bank of San Francisco[1] for business sector TFP, defined as output growth less the contribution of capital and labor (see, for example, Fernald (2014)). The TFP series is constructed as a percent change at an annual rate. The first row of Figure SA.8 presents estimates using $k = 1$ and $k = 2$, respectively, along with the observed data series. For each chart, we also display the estimate assuming a cycle component with no serial correlation (see Section SA.1). For both $k = 1$ and $k = 2$, the estimates with and without a serially correlated cycle are nearly indistinguishable. This is comforting as assuming the generality of a serially correlated cycle does not appear to be costly.

In the bottom left chart we show the trend estimate for either choice of k along with their associated 90% posterior coverage interval. We can observe that both the trend estimates and the uncertainty around them are similar for either choice. The median estimate of trend TFP growth hovers around 2% through the 1960s before a steep decline, falling to about 1.0% in 1980. In the 1980s and 1990s trend TFP growth partially reversed this fall before declining again in the last part of the sample. At the end of 2023, the estimated trend is about 0.5% although the uncertainty band is fairly wide.

[1] https://www.frbsf.org/economic-research/indicators-data/total-factor-productivity-tfp/

Figure SA.8: **Trend Estimates of Total Factor Productivity Growth.** This figure presents trend estimates of total factor productivity (TFP). The first row displays TFP growth along with the estimated trend for $k = 1$ and $k = 2$, respectively, based on the methodology introduced in Section 3. The bottom left chart displays the estimated trend for $k = 1$ and $k = 2$ along with the corresponding 90% posterior coverage interval. The bottom right chart replicates the top right chart along with a 90% posterior coverage interval. The sample period is 1947Q2–2023Q4.

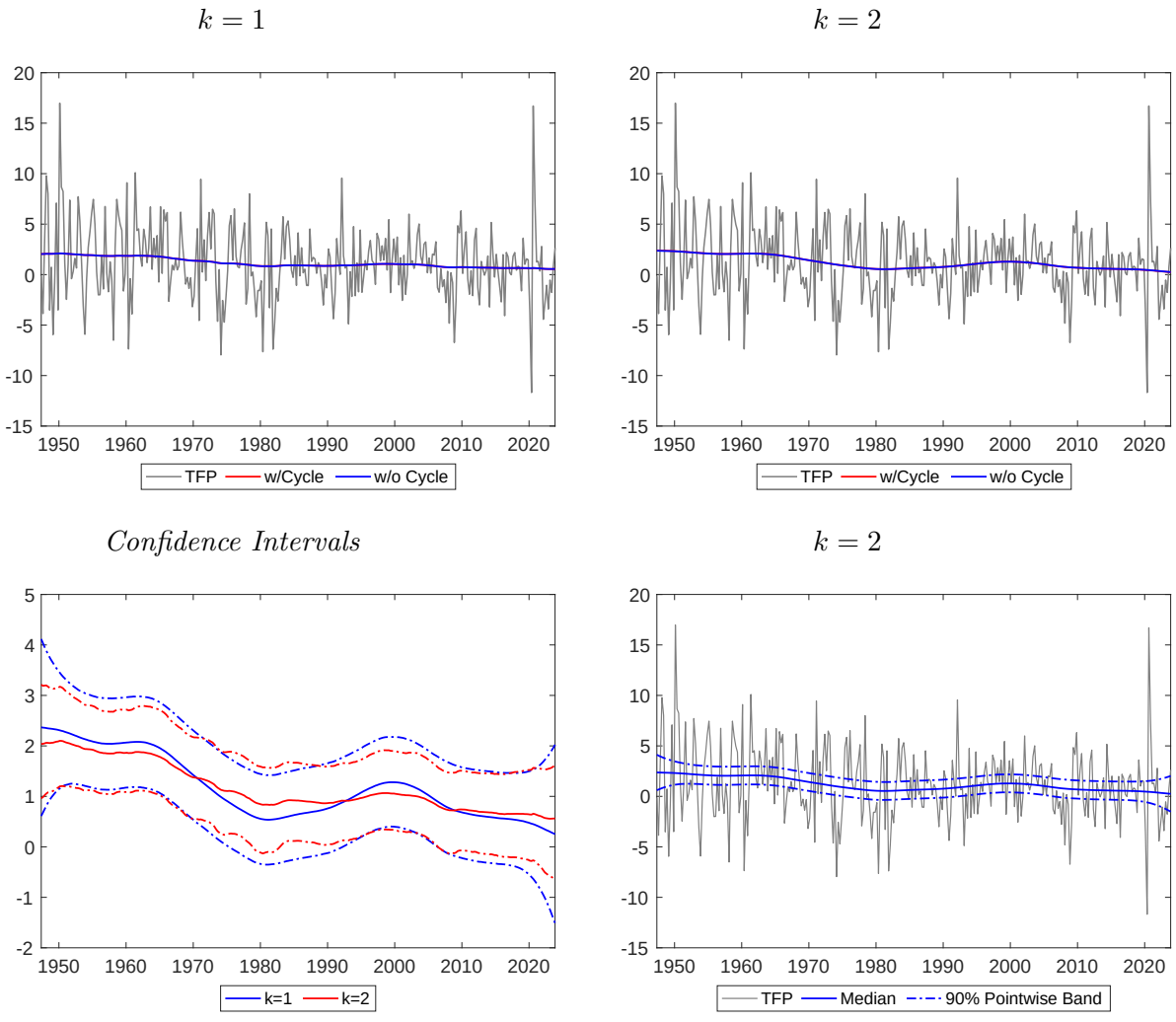

References

Fernald, J. G. (2014): "A Quarterly, Utilization-Adjusted Series on Total Factor Productivity," Working Paper 2012-19, Federal Reserve Bank of San Francisco.